Research Square

Preprints are preliminary reports that have not undergone peer review.
They should not be considered conclusive, used to inform clinical practice,
or referenced by the media as validated information.

Study on the Carrier Effect and Structure-Activity Relationship of Cobalt-Based Hydrogen Production Catalysts by Ammonia Reforming

Bin Guan

guanbin@sjtu.edu.cn

Shanghai Jiao Tong University

Zhongqi Zhuang

Shanghai Jiao Tong University

Lei Zhu

Shanghai Jiao Tong University

Chenyu Zhu

Shanghai Jiao Tong University

Tiankui Zhu

Shanghai Jiao Tong University

Shiying Chang

State Key Laboratory of Precious Metal Functional Materials

Jiangli Ma

State Key Laboratory of Precious Metal Functional Materials

Rong Wang

State-Local Joint Engineering Research Center of Precious Metal Catalytic Technology and Application

Dongxia Yang

Kunming Sino-Platinum Metals Catalyst Co.Ltd

Hanshi Qu

China FAW Group Co., Ltd.

Bingqian Tan

Wuxi Henghe EP Tech. Co., Ltd.

Zhen Huang

Shanghai Jiao Tong University

Research Article

Keywords: "ammonia-hydrogen" energy path, ammonia decomposition, nano CeO2 (Co/CeO2(N)), kinetic analysis

Posted Date: June 19th, 2026

DOI: https://doi.org/10.21203/rs.3.rs-9846962/v1

License: This work is licensed under a Creative Commons Attribution 4.0 International License.
Read Full License

Additional Declarations: No competing interests reported.

Version of Record: A version of this preprint was published at Research on Chemical Intermediates on September 24th, 2026. See the published version at https://doi.org/10.1007/s11164-026-06120-x.

Study on the Carrier Effect and Structure-Activity Relationship of Cobalt-Based Hydrogen Production Catalysts by Ammonia Reforming

Bin Guan* (guanbin@sjtu.edu.cn), Zhongqi Zhuang (zhongqizhuang@sjtu.edu.cn), Lei Zhu* (tonyzhulei@sjtu.edu.cn), Chenyu Zhu (zhuchenyu6@sjtu.edu.cn), Tiankui Zhu (zhutiankui@sjtu.edu.cn), Shiying Chang (shiying.chang@spmcatalyst.com), Jiangli Ma (amy.ma@spmcatalyst.com), Rong Wang (r-wang21@tsinghua.org.cn), Dongxia Yang (doris.yang@spmcatalyst.com), Hanshi Qu (quhanshi@faw.com.cn), Bingqian Tan (tanbingqian@henghe-ep.com), Zhen Huang (z-huang@sjtu.edu.cn)

Key Laboratory for Power Machinery and Engineering of Ministry of Education, Shanghai Jiao Tong University, Shanghai 200240, China

*****Corresponding author: Bin Guan

Dongchuan Road No.800, Min Hang District, Shanghai, P.R.China 200240

Tel.: +86 21 34206859; fax: +86 21 34205553.

E-mail: guanbin@sjtu.edu.cn

*****Corresponding author: Lei Zhu

Dongchuan Road No.800, Min Hang District, Shanghai, P.R.China 200240

Tel.: +86 21 34206859; fax: +86 21 34205553.

E-mail: tonyzhulei@sjtu.edu.cn

Abstract: To break through the bottleneck in hydrogen storage and transportation and advance the industrial application of the "ammonia-hydrogen" energy route, this study focuses on the carrier effect of cobalt-based non-precious metal ammonia decomposition catalysts. Through the deposition-precipitation method, cobalt-based catalysts loaded on different oxide carriers (CeO_2, La_2O_3, SiO_2, etc.) were prepared. Combined with XRD, TEM, XPS and other methods for characterization, the regulatory mechanism of the physical and chemical properties of the carriers on the structure and ammonia decomposition performance of the catalysts was systematically explored, and kinetic analysis and stability tests were carried out. The activity test shows that the chemical effect of the carrier has a much greater impact on the catalytic efficiency than the physical specific surface area. The cobalt-based catalyst loaded on nano CeO_2 ($Co/CeO_2(N)$) performed the best, with an ammonia conversion rate of 46.3% at 450℃ and approaching complete decomposition (94.2%) at 550℃, significantly superior to traditional Al_2O_3 and TiO_2 carrier catalysts. This research clarifies the correlation between carrier properties and the structure-activity relationship of cobalt-based catalysts, and confirms that nano CeO_2 can enhance catalytic performance through electronic regulation and the synergistic effect of basic sites, providing a theoretical foundation and technical support for the design and development of low-cost, high-stability ammonia decomposition catalysts.

Keywords: "ammonia-hydrogen" energy path, ammonia decomposition, nano CeO2 (Co/CeO2(N)), kinetic analysis.

1. Introduction

Energy is the cornerstone of human civilization's progress and the core driving force for industrialization, technological innovation, and economic growth. However, following centuries of rapid industrialization, the conventional fossil energy system centered on coal, oil, and natural gas is confronted with unprecedented challenges. On one hand, the non-renewability of fossil fuels has raised deep concerns about global energy supply security and long-term sustainability; on the other hand, the combustion of fossil fuels releases greenhouse gases, leading to global warming and frequent extreme weather phenomena, thereby exerting a severe hazard to the human living environment. In the face of this predicament, the transformation of the global energy system has become an irreversible historical trend, with the core being to break the long-term dominance of fossil fuels and build a clean, low-carbon, safe, and efficient new energy system [1, 2]. Against the backdrop of an increasing share of renewable energy, how to solve the problem of accommodating fluctuating power sources such as wind and solar energy, and how to achieve deep decarbonization in "difficult-to-decarbonize industries" such as steel, chemical engineering, and heavy-load transportation, have become two major challenges before us. Hydrogen, as a secondary energy source with a wide range of sources and combustion products being only water, is recognized as a key carrier for achieving the "carbon neutrality" goal due to its high energy density and the characteristic of interconnection across energy networks. Hydrogen is not only an ideal substitute for fossil fuels but also the "lubricant" of the future energy system. According to the "2050 Net Zero Emissions Roadmap" released by the International Energy Agency (IEA), by 2050, the share of low-carbon hydrogen and its synthetic fuels in terminal energy consumption needs to significantly increase to fill the emission gap that cannot be covered by electrification [3-5]. Although hydrogen occupies a core position in the "dual carbon" strategy, its physical and chemical properties determine the industrial dilemma of "easy to produce but difficult to store and transport". Hydrogen is the lightest element in nature, with a density extremely low (only 0.089 kg/m^3) under standard conditions, and its boiling point is as low as -252.9℃. These intrinsic properties render the efficient storage and long-distance transportation of hydrogen a major technical bottleneck that restricts its flow from the production side to the application side [6-10]. In summary, a single physical hydrogen storage method is difficult to simultaneously meet the industrial demands of high density, low cost, and high safety.

To address these challenges, the "indirect storage and transportation" route using liquid chemical

carriers or inorganic carriers has become a global research hotspot. Among these, NH_3 is considered the most promising "green hydrogen carrier" on account of its excellent hydrogen storage performance and well-developed industrial foundation.[11, 12]. Compared with hydrogen gas, ammonia has overwhelming advantages in the storage and transportation process. Firstly, ammonia has an extremely high hydrogen storage capacity, and the volume hydrogen content of liquid ammonia can reach 121 kg H_2/m^3, which is 1.7 times that of the same volume of liquid hydrogen. This means that in the same transportation space, ammonia can transport more hydrogen. Secondly, the liquefaction conditions of ammonia are relatively mild, requiring only cooling to -33℃ under one atmosphere pressure or pressurization to 10 bar at room temperature to liquefy, which makes its storage conditions far superior to liquid hydrogen (-253℃). Moreover, ammonia itself is a bulk chemical raw material with extremely mature synthesis, transportation, and distribution infrastructure worldwide. The existing ammonia transportation network (including pipelines, tankers, and transport ships) can be directly used for the blending of energy ammonia, significantly reducing the initial investment cost of infrastructure construction [13, 14].

However, to complete the last mile of the "ammonia-hydrogen" route, that is, to achieve efficient conversion from ammonia to hydrogen, there are still severe technical challenges. The ammonia decomposition reaction is a strongly endothermic reversible reaction, which generally requires a higher temperature or catalyst assistance to take place. Energy conversion efficiency directly determines the economic viability of the entire "ammonia-hydrogen" route. Current catalytic technologies struggle to meet the dual requirements of "low temperature, high activity" and "low cost" for this new route simultaneously [15]. Therefore, for the key link of "ammonia-hydrogen" energy conversion, developing non-precious metal ammonia decomposition catalysts with high activity and low cost, and designing efficient and compact reaction systems based on this, is the key to promoting hydrogen energy from concept to implementation, and is also the core driving force of this research paper.

The ammonia decomposition hydrogen production reaction (Equation 1) is a core technical link for releasing the chemical energy in ammonia and realizing the "ammonia-hydrogen" energy closed loop. From a thermodynamic perspective, this is a volume-expanding endothermic reversible reaction that requires external energy input to sustain the reaction.

$$NH_3(g) \leftrightarrows 0.5N_2(g) + 1.5H_2(g),\ \Delta H^\circ = +46.2\ kJ\cdot mol^{-1}_{NH_3} \quad (1)$$

Although the reaction has a spontaneous tendency at high temperatures, it is limited by the high N-H bond energy in ammonia molecules (391 kJ/mol), resulting in a significant energy barrier in the

kinetic process. Even at high temperatures, the reaction rate is extremely slow in the absence of a catalyst. Therefore, developing efficient, stable, and low-cost catalysts to remarkably reduce the reaction activation energy is the key to realizing rapid hydrogen production under mild conditions. The catalytic decomposition of ammonia mainly includes three approaches: thermal catalysis, electrocatalysis, and plasma-driven catalysis. Among them, thermal catalysis is the most mature and widely applied method [16]. This article mainly focuses on the thermal catalytic decomposition of ammonia. Currently, research on ammonia decomposition catalysts mainly focuses on two systems: one is represented by noble metal catalysts such as ruthenium, which have excellent low-temperature activity but are limited by resource scarcity and high cost [17-19]; the other is non-noble metal catalysts represented by nickel [20, 21], cobalt [22, 23], and iron, including bimetallic and multimetallic catalysts [24-26], which are low-cost and abundant in resources but usually require a relatively high reaction temperature (>600℃) to achieve an ideal conversion rate. How to achieve the optimal balance between catalytic activity and cost has become the main focus of current research in this field.

Among the current research systems for ammonia decomposition hydrogen production catalysts, ruthenium-based catalysts are recognized by both the academic and industrial communities as the activity benchmark for ammonia decomposition reactions [27, 28]. The dominant position of ruthenium in ammonia decomposition reactions is determined by its intrinsic electronic structure. Although the relative positions of different metals on the curve may vary slightly due to differences in computational models or catalyst supports, under typical reaction conditions (about 500℃), ruthenium is always at the top of the "volcano-shaped curve" of ammonia decomposition reactions, showing the optimal catalytic performance in ammonia decomposition [29-31]. Specifically, ruthenium has a moderate binding energy for nitrogen atoms (N*), which can effectively break the strong N-H bond and allow nitrogen atoms to recombine to form N_2 and desorb at a relatively low temperature, thus avoiding the "poisoning" of active sites [32].

In addition, the activity of ruthenium-based catalysts shows a high degree of structural sensitivity, mainly dependent on a special geometric configuration called the "B5 site" [33]. This step-like structure consisting of five ruthenium atoms is typically distributed on the edges of particles with a particle size of 2-5 nm, which can notably lower the energy barrier for nitrogen-nitrogen recombination. Thanks to this, optimized ruthenium-based catalysts (especially when modified with alkaline additives such as K, Cs or supported on CeO_2, CNTs, etc.) can reach near-thermodynamic equilibrium ammonia conversion

rates in the 400-450℃ temperature range [34, 35]. By comparison, conventional non-noble metal catalysts (including Ni, Fe) generally demand temperatures over 600℃ to attain the same degree. This significant temperature difference gives ruthenium-based catalysts a technical advantage in system start-up speed and energy consumption control [36].

Although ruthenium-based catalysts perform well at the laboratory scale, when the perspective is expanded to the gigawatt-scale (GW-scale) large-scale industrial hydrogen production scenario, their resource scarcity and high price constitute insurmountable macro barriers. Ruthenium is a platinum-group metal and ranks among the elements with the lowest abundance in the Earth's crust, with a global annual production extremely limited, only maintaining at around 30 tons, and highly concentrated in a few regions such as South Africa, with a very fragile supply chain. A technical economic assessment (TEA) of energy transition indicates that if only one 1 GW gas turbine power plant is converted to ammonia cracking hydrogen technology and uses the current ruthenium-based catalysts, this single project alone would consume about 10% of the global annual ruthenium production [37]. This means that the material basis of ruthenium simply cannot support the large-scale energy substitution demands on a global scale. This scarcity has led to sharp and expensive price fluctuations of ruthenium, directly driving up the costs of hydrogen production projects. To visually demonstrate its cost disadvantage, Table 1 compares the market prices and resource profiles of ruthenium with those of the main non-precious metal alternative elements (nickel, cobalt, iron) in recent years.

According to the data listed in the table, the price of ruthenium is more than 2,000 times higher than that of nickel and tens of thousands of times that of iron. Although the loading amount of ruthenium catalysts is usually low (1-5 wt%), the cost of the core metal still constitutes the overwhelming majority of the overall production cost of the catalyst [38]. In the highly cost-sensitive hydrogen economy model, this high initial investment seriously hinders the reduction of hydrogen production costs [39].

Table 1 Comparison of price, resources, and performance between ruthenium and non-noble metals (Fe, Ni, Co)

Comparison	Ru	Ni	Co	Fe

dimension				
Metal classification	Platinum group metals	Transition metals	Transition metals	Transition metals
Crustal abundance	Extremely low(~0.001 ppm)	Medium(~84 ppm)	Low (~25 ppm)	Extremely high(~56,300 ppm)
Market price(2025)	~32,000 /kg	~15 /kg	~45-50 /kg	~0.1-2.0 /kg
Price multiple (relative to Ni)	~2,100 times	1 time (base)	~3 times	~ 0.1 times
Price trend (2020-2025)	Significantly increased, with a rise of over 260% since 2020, and with extremely large fluctuations	Fluctuating downward, currently at a relatively low level	Significantly fluctuating, driven largely by battery demand	Long-term stable, low cost and easily accessible
Ammonia decomposition activation temperature	400 - 450℃[40]	600 - 700℃[36]	> 600℃[15]	> 700℃[15]
Main industries Challenges	High costs, risk of resource depletion	High temperature carbon deposition, poor low-temperature activity	Higher than Fe/Ni in cost, poor low-temperature activity	Too low activity, requires extremely high temperature

Given the high cost and scarce resource reserves of ruthenium-based catalysts, developing non-precious metal (mainly transition metals such as iron, cobalt, and nickel) catalysts with abundant

reserves, low prices, and superior activity has become a key core means to realize the industrial application of ammonia decomposition for hydrogen generation [41-43]. However, compared with precious metal ruthenium, non-precious metals have their own inherent limitations in thermodynamic properties and kinetic mechanisms, which are clearly demonstrated in the classic "volcano-shaped curve".

Iron, as the classic catalyst in the ammonia synthesis industry (Haber-Bosch process), performs unsatisfactorily in the ammonia decomposition reaction. According to the Sabatier principle, iron lies on the left-hand side of the volcano-type curve, and its core defect lies in its excessive affinity for nitrogen species [44, 45]. Density functional theory (DFT) calculations demonstrate that on Fe(110) and other face-centered planes, the adsorption energy of nitrogen atoms is as high as -1.70 eV to -1.82 eV, much higher than the optimal value of ruthenium (approximately -1.27 eV to -1.35 eV) [46]. This means that during the reaction, the active sites on the iron surface are easily occupied by high coverage of nitrogen atoms, hindering the subsequent adsorption of ammonia molecules and resulting in an extremely high energy barrier for nitrogen compound desorption. Therefore, pure iron catalysts usually require temperatures higher than 600℃ or even 700℃ to overcome the desorption energy barrier and achieve a higher conversion rate [47, 48]. Moreover, iron is prone to phase transformation into nitrogen-containing phases under rich ammonia atmospheres, forming thermodynamically stable but catalytically inert nitrides such as Fe4N or Fe3N, leading to a rapid decline in catalyst activity [49-51].

Using Co-Fe alloys can overcome this limitation of iron [51].The incorporation of cobalt lowers the d-band center of iron, weakens the strength of the Fe-N bond, and shifts the nitrogen adsorption energy toward the top of the volcano curve. Additionally, cobalt atoms act as a physical barrier within the lattice, which significantly restricts the diffusion of nitrogen atoms from the catalyst surface to the bulk phase. This effectively prevents the formation of detrimental bulk iron nitride and sustains the metallic active surface of the catalyst, ensuring its long-term catalytic activity [52, 53].

In comparison with iron, nickel generally lies on the right side of the volcano-shaped curve, and the nitrogen adsorption energy on the Ni (111) surface is lower than that of ruthenium [54]. This weaker interaction leads to a completely different kinetic bottleneck for nickel catalysts: on the one hand, the weak M-N bond (metal-nitrogen bond) makes it difficult for the catalyst to effectively polarize and break the N-H bond in the ammonia molecule, resulting in a higher first-step dehydrogenation activation energy; on the other hand, due to the weak adsorption, the coverage of the surface steady

intermediate species is low, and the probability of two nitrogen atoms meeting and undergoing complexation on the surface is significantly reduced [34]. To achieve the desired conversion rate, nickel-based catalysts usually need to operate at high temperatures (> 600°C)[55, 56], but this also leads to serious sintering problems, causing the high-activity step sites to disappear and the catalytic performance to significantly decline over time [57, 58].

Through in-depth analysis of iron and nickel, it can be concluded that non-precious metal catalysts are faced with a "dilemma": iron has a too strong binding, leading to poisoning, while nickel has a too weak binding, resulting in activation difficulties. According to the d-band theory, the position of the d-band center of transition metals shifts downward as their atomic number increases. Cobalt, which is located in Group 9, Period 4 of the periodic table, lies between iron and nickel. Correspondingly, its nitrogen adsorption energy falls between that of iron and nickel, and is closer to that of ruthenium [31, 54]. In Figures 1-2(c) and (e) of the volcano-shaped curve, the position of Co is close to the vertex Ru. This means that among non-precious metals, cobalt has a more suitable binding energy: it has a stronger ability to bind nitrogen than Ni, can effectively weaken the N-H bond; It has a weaker ability to bind nitrogen than Fe, and the nitrogen atoms on the surface formed during the reaction can be desorbed smoothly, avoiding surface poisoning and ensuring the smooth and rapid progress of the reaction [59].

From the perspective of electronic configuration, Co (3d7 4s2) and Ru (4d7 5s1) belong to the 9th column, and they have the same number of d-banded electrons. This intrinsic electronic structure similarity endows cobalt with the inherent potential to simulate the catalytic behavior of ruthenium. By finely regulating the d-band center of Co through alloying, carrier modification, etc., the adsorption strength of nitrogen can be optimized, making the nitrogen adsorption energy approach that of ruthenium or the theoretically predicted optimal level, thereby enhancing the catalytic activity and achieving the substitution of ruthenium [60].

Thanks to its inherent activity being higher than that of iron and nickel, cobalt-based catalysts are expected to achieve high conversion rates at lower temperature ranges (400-500°C). This characteristic enables it to better match the industrial waste heat utilization temperature, significantly reducing the energy consumption and equipment material costs of the hydrogen production system, and thus significantly reducing the average cost of obtaining hydrogen [40]. Therefore, cobalt is currently the most ideal active phase metal choice for achieving low-cost, low-temperature ammonia decomposition

for hydrogen production.

Therefore, this work focuses on the research of the carrier effect of catalysts, through experimental characterization to investigate the regulatory laws of different oxide carriers on the physical and chemical properties of the catalysts, revealing the structure-activity relationship between carrier characteristics and catalytic performance and optimizing the best carrier system. In supported metal catalysts, the carrier not only plays a physical framework role of dispersing and stabilizing the active components, but also through metal-carrier interactions, electron transfer effects, and surface acidity and basicity regulation mechanisms, improves the catalyst performance [61]. For cobalt-based ammonia decomposition catalysts, the physical and chemical properties of the carrier directly determine the electronic state of Co species and their adsorption and desorption behaviors of reaction intermediates (such as N atoms).

To screen out the most suitable carrier system and clarify its enhancement mechanism, The effect of various oxide carriers on the ammonia decomposition activity of supported cobalt catalysts was systematically explored, including traditional acidic carriers (Al_2O_3), inert/weakly acidic carriers (SiO_2, TiO_2), basic carriers (MgO), and rare earth oxide carriers (CeO_2, La_2O_3). By correlating catalytic activity with characterization results, the objective is to uncover the intrinsic nature of the carrier effect, thereby offering data support and a theoretical foundation for the subsequent design of efficient catalysts.

2. Experiment

To promote the development of non-precious metal catalysts, this study fabricated ammonia decomposition catalysts with various carriers and active components using the deposition-precipitation method. An evaluation method for catalytic activity and durability was established; a variety of physical and chemical characterization techniques, including XRD, TEM, BET, XPS, H_2-TPR, and CO_2-TPD, were comprehensively utilized to systematically analyze the phase structure, microstructure, and surface chemical properties of the materials. On a macroscopic scale, a numerical simulation model based on CFD was established to simulate the ammonia decomposition process in the reactor and the influence of thermal medium properties on hydrogen production, providing theoretical support for subsequent system integration design. Based on the above ideas, this chapter will specifically introduce the catalyst preparation process, performance evaluation, and physical and chemical characterization methods involved in this study.

2.1 Catalyst Preparation

This study prepared a series of non-precious metal and bimetallic alloy catalysts by means of the deposition-precipitation method, which loaded the active metal components onto different oxide carriers. This method utilized the uniform alkaline environment generated by the hydrolysis of urea at high temperatures to allow the active metal components to deposit slowly and uniformly on the surface of the carriers, achieving nanoscale dispersion of the active components. The specific preparation process is shown in Figure 1.

Firstly, 2.0 g of oxide carrier was weighed, and the corresponding metal nitrate precursors and precipitant urea were calculated and weighed according to a 10 wt% loading amount. The molar ratio of urea to metal elements was 20:1. For bimetallic catalysts, the molar ratio of the two metal elements was set at 1:1. The oxide carriers were CeO_2, La_2O_3, SiO_2, MgO, Al_2O_3, and TiO_2 powders. The metal precursors were the corresponding nitrate salts of the metals, including $Co(NO_3)_2{\cdot}6H_2O$, $Ni(NO_3)_2{\cdot}6H_2O$, $Fe(NO_3)_3{\cdot}9H_2O$, and $Mn(NO_3)_2{\cdot}4H_2O$.

An appropriate amount of deionized water was used to dissolve the carrier and metal precursors; after thorough stirring to achieve uniform mixing, the precipitant was added sequentially. The mixture was placed in a constant temperature magnetic stirring water bath at 80℃ and reacted for 8 hours under continuous magnetic stirring to complete the precipitation process.

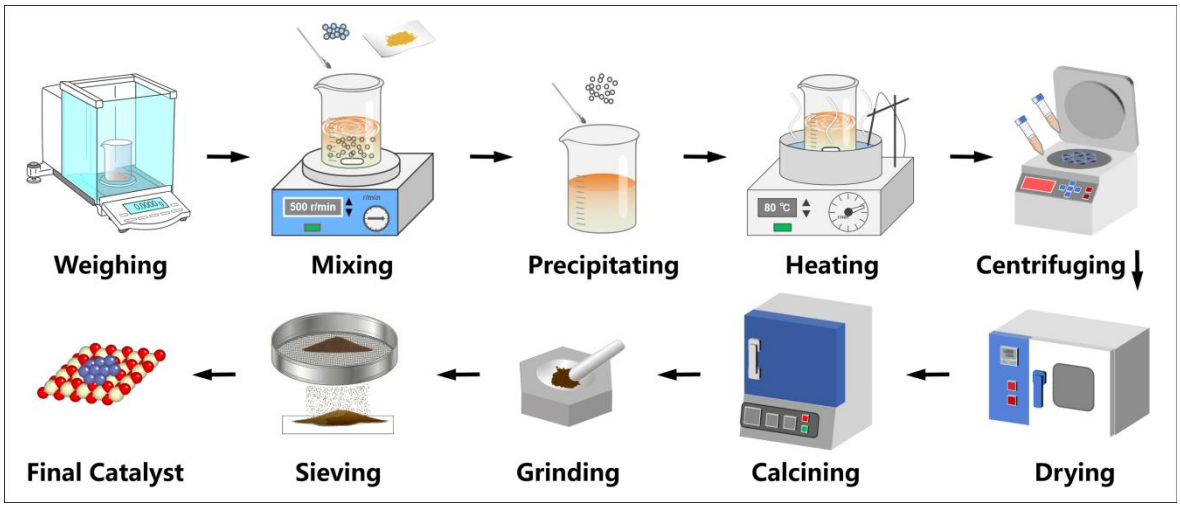


Fig.1 Schematic diagram of the catalyst preparation process

After the suspension liquid is cooled to room temperature, the upper clear liquid is removed by centrifugation. The bottom precipitate is placed in an oven at 80℃ to dry overnight to remove the

physically adsorbed water, and then it is calcined in a muffle furnace at 600℃ for 2 hours to form stable metal oxide active phases. Finally, after grinding and sieving the calcined samples, particles with a particle size of 40 to 80 mesh are selected to serve as the final catalyst.

In addition, based on the same process, 5 wt% and 20 wt% Co/La_2O_3 samples were prepared, as well as Co-Ni/CeO_2(N) samples with molar ratios of 1:3 and 3:1 to compare the effects of loading amount and alloy ratio on catalytic performance.

To facilitate the expression and discussion in the subsequent chapters, this paper uniformly names the prepared catalysts in the format of "active component/substrate (N)". The suffix "(N)" represents that the used substrate is in nano size (Nano), and if there is no this suffix, it is assumed to be in micrometer size. For example, "Co/CeO_2(N)" represents a catalyst with Co as the active component and nano CeO_2 as the substrate. Moreover, if not specified otherwise, the total loading amount of the active metal in the catalyst is assumed to be 10 wt%, and if it is a bimetallic catalyst, the molar ratio is 1:1.

2.2 Performance Evaluation and Physical and Chemical Characterization Methods of Catalysts

The catalyst activity evaluation system primarily consists of three parts: a gas control unit, an ammonia decomposition reaction unit, and a product analysis unit, which is shown in Figure 2. The gas control unit includes standard gas cylinders, pressure reducers, precision pressure gauges, and gas flow meters, which are used to precisely control the flow rate of reaction raw materials; the core of the reaction unit is a tube furnace equipped with a program temperature rise and temperature control module, and the reactor is made of quartz glass tubes; the product analysis unit is equipped with an online gas chromatograph (GC) for real-time detection of tail gas components.

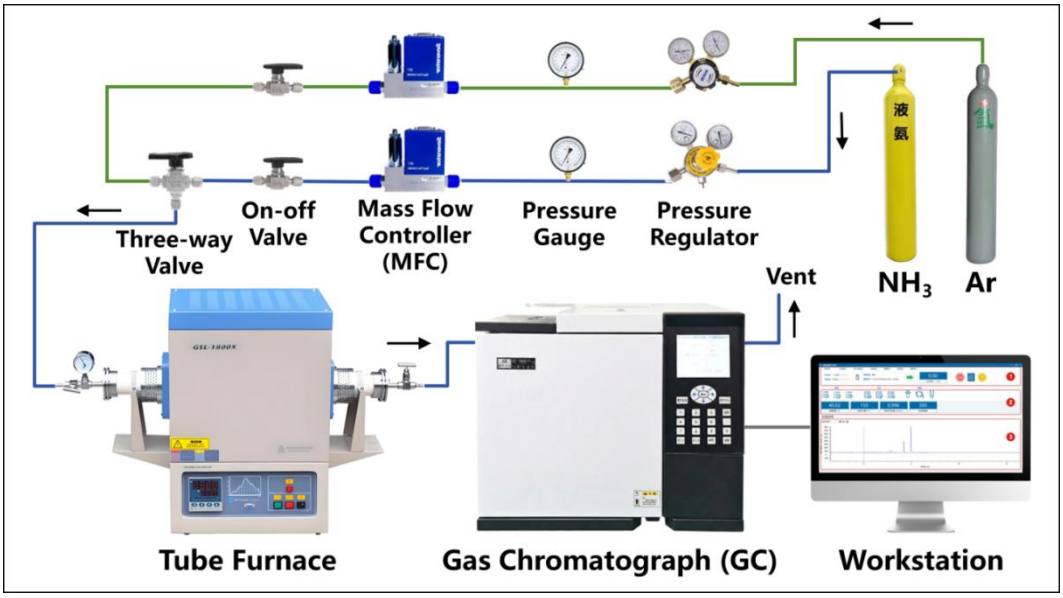


Fig.2 Schematic diagram of the ammonia decomposition catalyst activity evaluation system

The experimental raw gas used was high-purity ammonia gas with a purity of 99.99%. Each time, 0.5 g of catalyst powder was weighed and filled into the constant temperature zone of the reaction tube, and the ammonia flow rate was set at 1 L/h, resulting in a mass specific hydrogen production rate (WHSV) of 2,000 mL/(h·g_{cat}). Before the formal activity test, the bed temperature was raised to 550℃ and maintained for 1 hour under a pure NH_3 atmosphere for pre-reduction treatment and in-situ activation of the catalyst.

After the pre-treatment was completed, the activity was evaluated at different temperature points according to the cooling or heating procedures. To ensure that the reaction reached thermodynamic and kinetic equilibrium, the residence time at each temperature point was more than 17 minutes. The method of taking two samples at each temperature point and averaging them was used to reduce experimental errors.

The ammonia decomposition conversion rate was calculated based on the hydrogen concentration detected by the gas chromatograph. Given that the ammonia decomposition reaction (Equation 1) is a volume expansion reaction process, the total number of moles of gas before and after the reaction will increase as the conversion rate increases. Based on the reaction stoichiometry and material balance principles, the calculation formula for ammonia conversion rate (X_{NH3}) and the outlet hydrogen mole fraction (y_{H2}) is as follows:

$$X_{NH_3} = \frac{2y_{H_2}}{3-2y_{H_2}} \times 100\% \quad (2)$$

Based on the data of ammonia decomposition and conversion rates at different temperatures, the reaction rate constant (k) of the catalyst can be calculated, and the apparent activation energy (Ea) and pre-exponential factor (A) of the reaction can be determined using the Arrhenius formula. This allows for an evaluation of the intrinsic activity of the catalyst from a kinetic perspective. The catalytic decomposition reaction of ammonia is generally in the form of a zero-order reaction kinetics model, meaning that the reaction rate does not change with the concentration of reactants, but is only affected by the number of active sites on the catalyst surface and temperature. The formula for calculating the reaction rate constant k is as follows:

$$k = \frac{F_{NH_3} X_{NH_3}}{m_{cat}} \quad (3)$$

In the equation, F_{NH3} denotes the molar flow rate of ammonia at the reactor inlet, and m_{cat} stands for the catalyst loading mass.

According to Arrhenius' law, the reaction rate constant k has an exponential relationship with the reaction temperature T:

$$k = Ae^{-E_a/RT} \quad (4)$$

In the equation, R denotes the ideal gas constant, and T represents the thermodynamic temperature of the reaction.

To solve the kinetic parameters through linear regression, the natural logarithm is taken on both sides of the equation, converting it into a linear form:

$$\ln k = -\frac{E_a}{R}\frac{1}{T} + \ln A \quad (5)$$

Plot the Arrhenius curve with 1000/T as the abscissa and lnk as the ordinate. Use the least squares method to perform linear fitting on the experimental data points. Based on the slope and intercept of the obtained straight line, the kinetic parameters Ea and A can be calculated.

3. Results and Discussion

3.1 Optimization of Active Component Loading

Before systematically investigating the effect of the carrier, the loading amount of the active component cobalt (Co) was first optimized to determine the optimal metal loading ratio. Figure 3 shows the ammonia decomposition rates of Co/La_2O_3 catalysts with different cobalt loading amounts (5 wt%, 10 wt%, 20 wt%) within the temperature range of 350 to 650°C. The ammonia is of high purity

and the mass flow rate (WHSV) is 2000 mL/(h·g_{cat}).

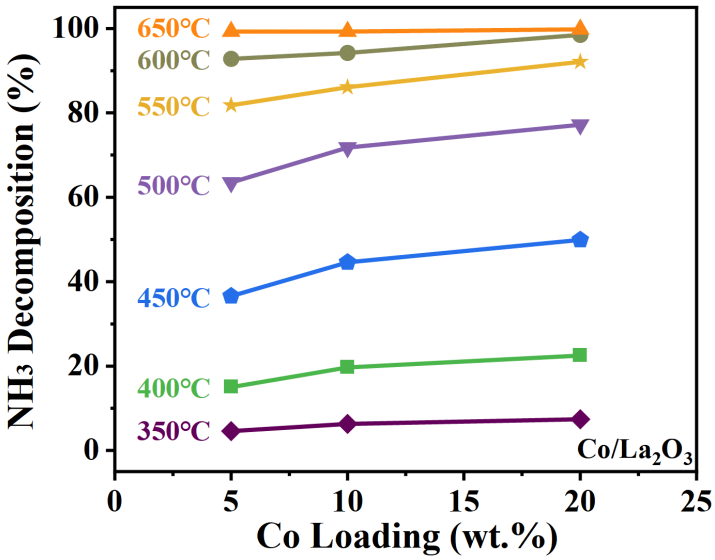


Fig.3 Effect of cobalt loading on ammonia decomposition activity at different temperatures

The experimental results show that as the cobalt loading increases, the ammonia decomposition activity of the catalyst exhibits a non-linear growth trend. At high temperatures (700°C) or low temperatures (350°C), due to complete decomposition or the beginning of decomposition, the influence of the loading amount on the ammonia decomposition rate is relatively small. In the medium-temperature range (e.g., 450°C), when the loading amount increases from 5 wt% to 10 wt%, the ammonia conversion rate significantly increases from 36.6% to 44.6%, indicating that increasing the density of active sites can effectively overcome the reaction kinetics limitation. However, when the loading amount is further increased to 20 wt%, the increase in conversion rate slows down significantly (only increasing to 49.9%). This marginal benefit diminishing phenomenon is mainly attributed to the aggregation effect of metal particles: excessive loading often leads to an increase in cobalt particle size and a decrease in dispersion, thereby reducing the atomic utilization rate per unit mass of metal.

Therefore, a loading amount of 10 wt% ensures a high catalytic efficiency while avoiding the use of excessive metal, which can more prominently highlight the influence of different carriers on catalytic performance. To control variables for easier comparison, the total metal loading in the subsequent studies of this paper is all 10 wt%.

3.2 Performance Comparison of Ammonia Decomposition Catalysts on Different Supports

This section selects several typical oxide supports and their specifications (nanometer/micrometer)

for comparison. Figure 4 shows the curves of ammonia decomposition conversion rate of each catalyst with temperature changes (350 - 700°C). The cobalt-based catalysts loaded on different supports show significant differences in activity.

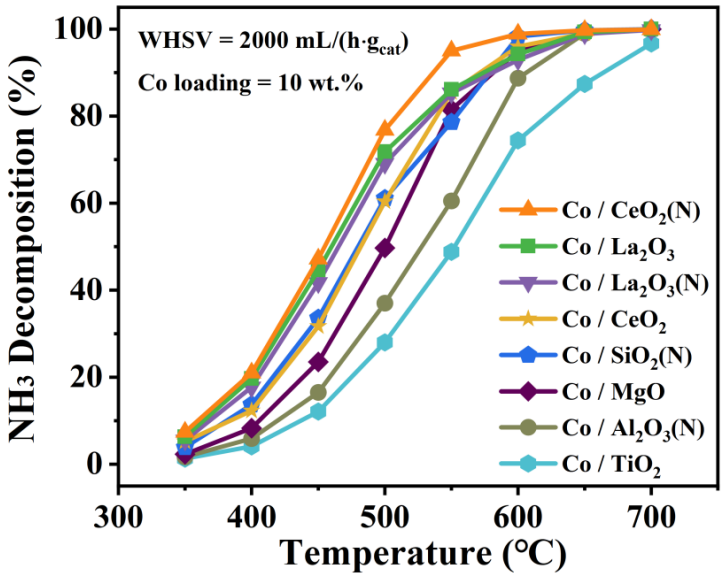


Fig.4 Ammonia decomposition activity of cobalt-based catalysts supported on different carriers

From the overall trend, the ammonia conversion rate of all samples increased with the rise in temperature, presenting a typical "S" curve. According to the experimental data, the activity sequence of the various catalysts was approximately: $Co/CeO_2(N) > Co/La_2O_3 > Co/La_2O_3(N) > Co/CeO_2 > Co/SiO_2(N) > Co/MgO > Co/Al_2O_3(N) > Co/TiO_2$.

The data clearly reflect that the catalysts loaded with rare earth oxides (CeO_2 and La_2O_3) have the most excellent low-temperature activity. Taking $Co/CeO_2(N)$ as an example, the conversion rate of this catalyst reached 46.3% at 450°C, significantly higher than that of Co/MgO (23.5%) and $Co/Al_2O_3(N)$ (16.5%) at the same temperature. As the temperature further increased to 550°C, the activity difference further widened: the conversion rate of $Co/CeO_2(N)$ soared to 94.2%, achieving complete ammonia decomposition, and the hydrogen production rate was approximately 2.8 $m^3/(h \cdot kgcat)$ at this time; in contrast, the traditional $Co/Al_2O_3(N)$ catalyst had a conversion rate of only 60.5%, while Co/TiO_2 performed the worst, at only 48.8%.

It is worth noting that although Al_2O_3 usually has a larger specific surface area, the activity of the Co catalysts loaded on it is at a relatively low level, suggesting that in the ammonia decomposition reaction, the chemical properties of the carrier (such as redox properties, acidity and basicity) play a

more crucial role than the simple physical surface area. The reason why Co/CeO_2(N) performed the best may be attributed to the unique oxygen storage and release ability of CeO_2 and the strong metal-carrier interaction, which will be discussed in detail in the subsequent characterization.

3.3 Chemical Reaction Kinetic Analysis

To further quantify the carrier effect from a kinetic perspective, the relationship between reaction rate and temperature was fitted based on the Arrhenius equation: by plotting the ln(r) against 1000/T curve (Figure 5), the apparent activation energy (Ea) of each catalyst was calculated, as shown in Table 5. Within the examined temperature range (350-500℃), the ln(k) of all samples and 1000/T showed a good linear relationship, indicating that the ammonia decomposition reaction under these experimental conditions follows the typical zero-order reaction kinetic characteristics.

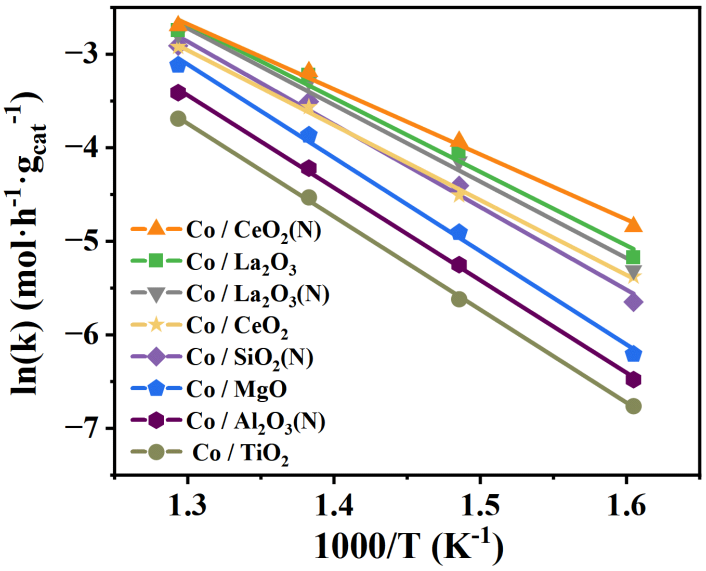


Fig.5 Arrhenius plots for catalysts supported on different carriers

As shown in Table 2, the apparent activation energy values of different catalysts are distributed within a relatively wide range of 57.90 - 83.01 kJ/mol, and their changing trend shows a strong negative correlation with the activity test results. That is, the higher the activity, the lower the activation energy.

Among all the samples, Co/CeO_2(N) once again demonstrated its superiority. Its apparent activation energy was only 57.90 kJ/mol, which was significantly lower than that of Co/Al_2O_3(N) (82.21 kJ/mol) and Co/TiO_2 (82.69 kJ/mol). The lower activation energy means that the CeO_2 carrier greatly reduces the energy barrier of the reaction, making the dehydrogenation of ammonia molecules

407 at the active sites or the desorption of nitrogen atoms much easier.

408

409 Table 2. Reaction activity parameters of catalysts supported on different carriers

Type of catalyst	E_a ($kJ \cdot mol^{-1}$)	A ($mol \cdot h^{-1} \cdot kg_{cat}^{-1}$)
$Co/CeO_2(N)$	57.90	5.87×10^2
Co/La_2O_3	65.49	1.92×10^3
$Co/La_2O_3(N)$	68.08	2.76×10^3
Co/CeO_2	66.59	1.73×10^3
$Co/SiO_2(N)$	73.53	5.61×10^3
Co/MgO	83.01	1.93×10^4
$Co/Al_2O_3(N)$	82.21	1.23×10^4
Co/TiO_2	82.69	9.78×10^3

410

411 Overall, the activation energies of the catalysts loaded with rare earth oxide supports (CeO_2, La_2O_3)
412 are generally lower than those of inert supports (such as SiO_2) and acidic/strongly basic supports
413 (Al_2O_3, MgO). Additionally, although Co/MgO has the highest pre-exponential factor (1.93×104), this
414 is mainly due to the "compensation effect" in the kinetics, and its excessively high activation energy
415 (83.01 kJ/mol) remains the dominant factor limiting its low-temperature performance.

416 In conclusion, the kinetic analysis further confirms that the core of the carrier effect lies in the
417 regulation of the reaction energy barrier. Nanoscale CeO_2 effectively reduces the activation energy of
418 the ammonia decomposition reaction due to its unique electronic properties.

419 3.4 Phase composition and microstructure of the catalysts

420 3.4.1 Element content analysis

421 Before exploring the relationship between the structure and activity of the catalysts, it is crucial to
422 accurately determine the actual content of the active components. In this study, inductively coupled
423 plasma atomic emission spectrometry (ICP-OES) was used to conduct quantitative analysis of all
424 prepared catalysts, and the specific results are listed in Table 3.

425

426 Table 3. ICP results of catalysts supported on different carriers

Type of catalyst	Loading amount of cobalt (wt%)
$Co/CeO_2(N)$	6.46
Co/La_2O_3	9.66
$Co/La_2O_3(N)$	11.25
Co/CeO_2	5.04
$Co/SiO_2(N)$	8.30
Co/MgO	9.34
$Co/Al_2O_3(N)$	10.07
Co/TiO_2	7.50

Although the loading amount was uniformly set at 10 wt% during the preparation process in this study, the final test results showed that due to the differences in the surface properties of different carriers (such as specific surface area) and the physical and chemical changes during the impregnation and calcination processes, the actual cobalt content of each sample exhibited a certain fluctuation range. Among them, the actual loading amounts of $Co/Al_2O_3(N)$, Co/La_2O_3, and Co/MgO were highly consistent with the theoretical values, indicating that these carriers have a good adsorption retention ability for the cobalt precursor.

However, the rare earth cerium-based catalyst that exhibited the best activity had a relatively lower actual cobalt loading, with $Co/CeO_2(N)$ being 6.46 wt% and micro-sized Co/CeO_2 being only 5.04 wt% in this case. In fact, during the preparation process, it could be observed that after precipitation and solid-liquid separation, the filtrate color of CeO_2 as the carrier remained pink, indicating that a considerable amount of cobalt ions did not precipitate but were lost in the solution in this form. In the study, attempts were also made to increase the dosage of the precipitant, but no significant improvement was observed. This might be attributed to the relatively small specific surface area of CeO_2, which limited its adsorption capacity for cobalt ions, or the surface charge properties causing electrostatic repulsion of ion adsorption.

However, this set of data precisely reveals a highly persuasive fact: although the actual active metal content of $Co/CeO_2(N)$ (6.46 wt%) is much lower than that of $Co/Al_2O_3(N)$ (10.07 wt%), its

catalytic activity is significantly better than the latter. This strongly proves that the CeO_2 carrier does not enhance performance simply by increasing the number of active sites, but rather through unique electronic effects significantly improves the intrinsic catalytic efficiency (TOF) per cobalt atom, this "less but better" characteristic has important engineering significance for catalyst optimization and cost reduction.

3.4.2 Porous Structure and Specific Surface Area

To deeply explore the potential influence of the physical texture of the carrier on the catalyst performance, this study used N_2 physical adsorption-desorption technology to systematically characterize the specific surface area, pore volume, and average pore diameter of the series of catalysts prepared. To more accurately reflect the pore characteristics of the materials, the total pore volume (Vp) in this study was uniformly calculated based on the BJH adsorption data, while the average pore diameter (Dp) was determined based on the BJH desorption data. The detailed results are summarized in Table 4.

Table 4. Textural properties of catalysts supported on different carriers

Type of catalyst	BET specific surface area (S_{BET}) (m^2/g)	Total pore volume (V_p) (cm^3/g)	Average pore diameter (D_p) (nm)
$Co/CeO_2(N)$	15.898	0.066	12.241
Co/La_2O_3	18.965	0.099	20.133
$Co/La_2O_3(N)$	19.122	0.110	3.819
Co/CeO_2	21.915	0.096	14.353
$Co/SiO_2(N)$	184.647	1.038	20.147
Co/MgO	69.165	0.475	23.894
$Co/Al_2O_3(N)$	379.835	1.373	13.257
Co/TiO_2	13.872	0.065	20.313

It is not difficult to observe from the data in Table 4 that the catalysts constructed on different carriers exhibit significant differences in their structural properties. The nano-carriers represented by $Co/Al_2O_3(N)$ show an extremely developed pore structure, with a BET specific surface area of up to

379.84 m^2/g and a total pore volume of 1.37 cm^3/g. Theoretically, such a huge specific surface area can provide extremely abundant attachment sites for active metals, facilitating the highly dispersed state of Co species. In contrast, the $Co/CeO_2(N)$ with the best catalytic activity has a much smaller specific surface area of only 15.90 m^2/g and a pore volume of approximately 0.07 cm^3/g. Moreover, $Co/La_2O_3(N)$ shows a very small average pore diameter of 3.82 nm, which may be related to the special packing density of its nanocrystalline grains.

Another counter-intuitive point is that the BET specific surface area of $Co/CeO_2(N)$ in the study (15.90 m^2/g) is slightly lower than that of Co/CeO_2 (21.92 m^2/g), which seems to contradict the conventional understanding that "nanomaterials have high specific surface areas". This phenomenon is mainly attributed to the extremely high surface energy of nano-CeO_2 and its thermal instability during the high-temperature sintering process. Due to the nanocrystalline particles being in a thermodynamic metastable state, they are prone to undergo intense agglomeration and sintering during the sintering process, causing the originally open inter-particle pores to collapse or close. Additionally, the loaded Co species may preferentially fill the small interstitial channels between the nanocrystalline particles, further reducing the effective specific surface area. On the contrary, although the micro-sized CeO_2 has larger crystal grains, its framework structure becomes more rigidly stable under heat treatment, thus retaining a relatively larger number of pore structures.

To more intuitively understand the physical meaning of these data, Figure 6 further presents the adsorption-desorption isotherms and pore size distribution curves of each catalyst.

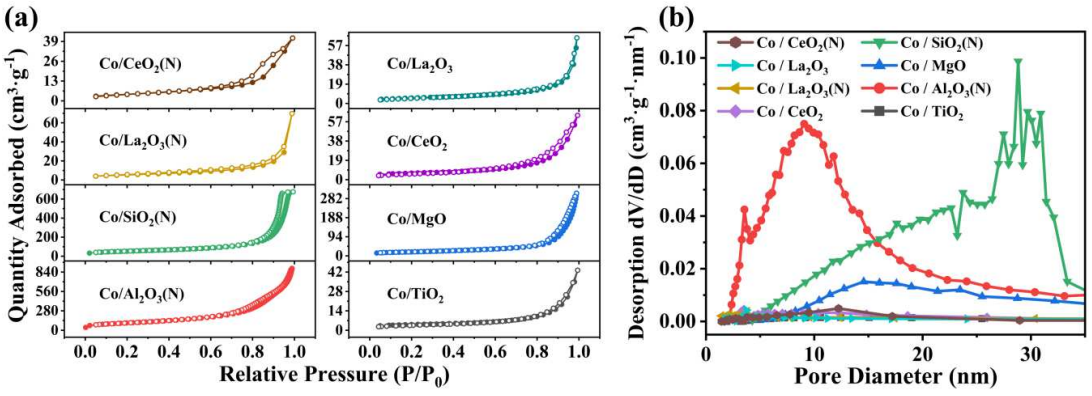


Fig.6 (a) N_2 adsorption-desorption isotherms and (b) BJH pore size distribution curves of catalysts with different supports

According to the IUPAC classification, the isotherms of all samples exhibit typical IV-type

characteristics, and a significant hysteresis loop appears within the relative pressure (P/P0) range of 0.4 - 1.0. This indicates that all the catalysts have mesoporous structures.

However, the shape of the hysteresis loop reveals significant differences in the pore geometric characteristics. Co/SiO_2(N) shows a more typical H1-type hysteresis loop feature, indicating a relatively regular pore structure, possibly formed by the close packing of spherical particles, with a relatively concentrated pore size distribution; Co/CeO_2(N) has a hysteresis loop more similar to the H1-type hysteresis loop, but also has some features of the H3-type hysteresis loop, indicating a relatively regular pore structure and a relatively concentrated pore size distribution; the other catalysts show H3-type hysteresis loop features, and this hysteresis loop is usually related to the slit pores formed by the stacking of plate-like particles, and the adsorption branches do not have a significant adsorption plateau when approaching the saturated vapor pressure, indicating the presence of large pores or inter-particle stacking pores in the material, and the pore structure is relatively irregular.

The pore size distribution curve in Figure 6(b) further confirms this. Co/SiO_2(N) shows the narrowest and sharpest distribution peak, centered at approximately 28 nm, indicating a relatively uniform mesoporous structure; while the pore size distribution of Co/CeO_2(N) is slightly broader, with the main peak at approximately 12 nm, the pore size distribution is neither particularly concentrated nor particularly dispersed, between Co/SiO_2(N) and other catalysts, which also indicates that the dispersion of the Co species on the surface is better and more uniform, this moderate pore size distribution situation may be one of the reasons for its optimal activity; the pore size distribution of the other catalysts shows greater irregularity, with a tendency to extend to the large pore region, this wide distribution feature is related to the disordered pore structure formed by the particle stacking. It should be noted that the small peaks around 3.8 nm in some samples are usually attributed to the "stretching strength effect (TSE)" caused by the nitrogen adsorption test, and do not represent the true microporous structure.

Based on the analysis results of Table 4 and Figure 6, an extremely important anomaly was observed. Co/Al_2O_3(N) with the largest specific surface area (379.84 m^2/g) does not exhibit the highest catalytic activity, but rather Co/CeO_2(N) with a specific surface area only 1/24 of it has an advantage. This result strongly proves that for the ammonia decomposition reaction, the physical texture (such as specific surface area) is not the only or dominant factor determining the catalytic performance.

3.4.3 Crystal Phase Structure Analysis

To determine the phase composition of the catalysts and the crystallization state of the active components on the carrier surface, X-ray diffraction (XRD) characterization was performed on each carrier-loaded cobalt-based catalyst after calcination, as shown in Figure 7.

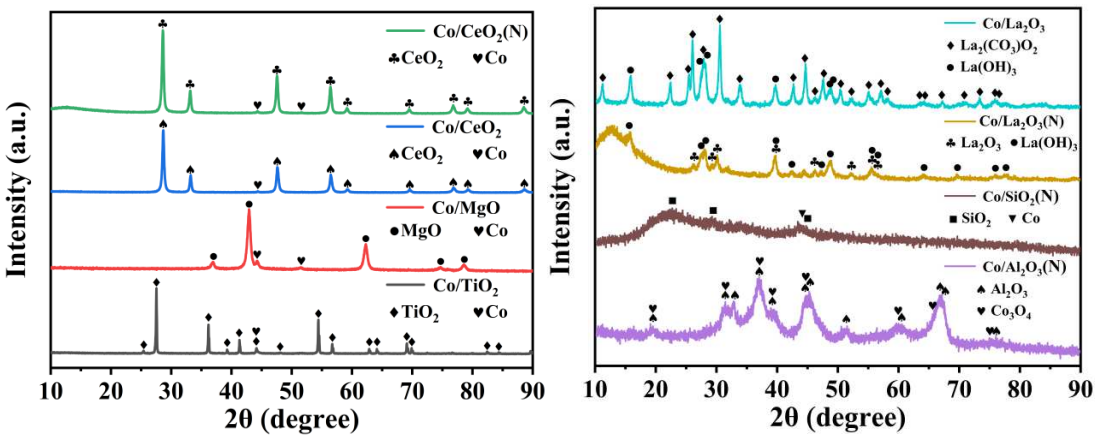


Fig.7 XRD patterns of catalysts supported on different carriers

From the spectra, it can be clearly observed that different carrier systems exhibit completely different diffraction characteristics. The peak intensity is higher in the left graph, and the peak shape is clearer, indicating that the crystallinity of the catalyst particles is higher. While the several substances in the right graph have lower crystallinity, resulting in a broader peak shape.

For the Co/CeO_2(N) sample that shows the best activity, its XRD spectrum is dominated by the characteristic peaks of the carrier. Sharp and intense diffraction peaks with extremely high intensity appear near 2θ values of 28.5°, 33.1°, 47.5°, and 56.3°, which perfectly correspond to the (111), (200), (220), and (311) crystal planes of the cubic fluorite structure CeO_2 (PDF#04-003-6947), indicating that the nano-CeO_2 carrier has excellent crystallinity. Most importantly, on the corresponding curve in this spectrum, there are almost no obvious characteristic diffraction peaks belonging to the single Co element or other Co species, while relatively obvious peaks of Co single species are observed in Co/MgO and Co/TiO_2. Considering that ICP analysis has confirmed that this sample contains approximately 6.5 wt% of cobalt, the absence of this diffraction signal strongly indicates that the Co species do not undergo large-scale agglomeration on the CeO_2 surface, but exist in a highly dispersed microcrystalline or amorphous cluster form, or even may partially enter the CeO_2 lattice to form a solid solution. This highly dispersed state may be attributed to the abundant oxygen vacancies on the CeO_2 surface, which strongly anchor the cobalt atoms.

In the XRD spectra of the Co/La_2O_3 series samples, in addition to the expected characteristic peaks of calcium oxide (La_2O_3), a clear diffraction signal of $La_2(CO_3)O_2$ (carbonated calcium oxide) was observed. The appearance of this phase is not a synthetic impurity but is determined by the inherent physical and chemical properties of the La_2O_3 carrier. As the strongest alkaline material among rare earth oxides, La_2O_3 has extremely strong hygroscopicity and affinity for acidic gases. During the storage or sample preparation of the catalyst in the air, La_2O_3 is easily chemically adsorbed and reacts with atmospheric CO_2 and H_2O ($La_2O_3 + CO_2 \rightarrow La_2(CO_3)O_2$), generating thermodynamically relatively stable monoclinic or hexagonal phase carbonated calcium oxide in situ.

Although this carbonation process to some extent alters the phase structure of the carrier, this "air sensitivity" precisely corroborates that the surface of this carrier has extremely rich strong alkaline sites. In the ammonia decomposition reaction mechanism, the abundant surface alkaline sites are generally considered to facilitate the transfer of electrons to the metal cobalt, thereby promoting the activation and breakage of N-H bonds. Therefore, the presence of $La_2(CO_3)O_2$ is not only direct evidence of the high alkalinity of the lanthanide-based material, but also may be the structural basis for its specific catalytic behavior under reaction conditions.

In contrast, the spectrum of $Co/Al_2O_3(N)$ shows broader diffraction peaks, which is consistent with the relatively lower crystallinity of γ-Al_2O_3. It should be noted that the broad shoulder peaks near $2\theta \approx 37°$ and 46° often overlap with the signals of the spinel phase Co_3O_4 or cobalt aluminum oxide CoAl2O4. Although this peak broadening also implies a certain degree of dispersion, combined with its peak position and the relatively low catalytic activity, it is more likely to form surface spinel species that are difficult to reduce, resulting in a decrease in the number of active sites.

For Co/TiO_2, the spectrum shows extremely sharp and complex diffraction peaks, mainly corresponding to the high crystallinity characteristics of the anatase and rutile mixed phase. However, this highly crystalline carrier fails to effectively disperse the active components, and its low specific surface area (only 13.9 m^2/g) limits the spread of the Co species, resulting in poor overall catalytic activity of the catalyst. In conclusion, the XRD characterization results, from the perspective of crystallography, confirmed that although the CeO_2 carrier has a high degree of crystallinity itself, it can achieve "nanoscale" or "cluster-level" high dispersion of the active component cobalt through unique interfacial interactions, thereby exposing more active sites. This perfectly explains why $Co/CeO_2(N)$ still exhibits the highest ammonia decomposition catalytic performance despite not having a dominant

specific surface area.

3.4.4 Microscopic Morphological Characteristics

To further reveal the dispersion state of the active component on the carrier surface and the contact characteristics of the metal-carrier interface at the microscopic scale, transmission electron microscopy (TEM), high-resolution transmission electron microscopy (HRTEM), and energy dispersive X-ray spectroscopy (EDS) surface scanning were conducted on the representative catalysts (Co/CeO_2(N), Co/CeO_2, Co/La_2O_3). Figure 8 shows the microscopic morphology of these three catalysts from top to bottom.

For the Co/CeO_2(N) sample with the best activity (Figure 3-6(a)), the TEM image at the middle position shows that the nano-CeO_2 carrier mainly presents an irregular polyhedral structure with a particle size of approximately 20 nm, and the cross-section is mostly spherical. At lower magnifications, no large dark aggregates of high size are observed on the carrier surface, indicating that the active metal cobalt is anchored on the carrier with an extremely high dispersion, which is highly consistent with the result that no obvious cobalt peak was detected in the XRD.

The HRTEM image on the left further reveals the details of the metal-carrier interface. Clearly visible in the image are multiple lattice stripes closely intertwined, with a lattice spacing of 0.312 nm corresponding to the (111) crystal plane of CeO_2; while the adjacent nano-clusters show a stripe spacing of 0.215 nm, corresponding to the (220) crystal plane of CoO. Additionally, CeO_2's (220) crystal face stripes and the (220) crystal face of the metal Co in close contact are also observed. In other areas of the sample, the (111) crystal face stripes of Co with the highest density are clearly captured. At the interface between cobalt and cerium oxide, the lattice stripes show obvious continuity or epitaxial growth characteristics, providing direct geometric evidence for the existence of strong metal-carrier interaction. This tight interface contact is conducive to electron transfer during the reaction process and the migration of oxygen species.

The EDS elemental surface scan on the right shows that the O region overlaps highly with Co and Ce (not shown in the figure), confirming the high overlap and relatively uniform distribution of the three elements Co, Ce, and O in the microscopic area, without obvious Co enrichment areas, again confirming the excellent dispersion ability of the nano-oxide cerium carrier for the Co species. In the high-resolution image, a key detail can be clearly captured: CeO_2 not only serves as a supporting substrate, but its surface species even show a tendency to migrate to the surface of the cobalt particles,

forming a layer of tightly adhered nano-thin layer. This unique coating structure is the direct evidence of strong metal-carrier interaction in the geometric morphology. It is like a protective film, not only physically fixing the cobalt particles, effectively inhibiting their migration and sintering in the high-temperature reaction, but also constructing the maximum metal-oxide interface, providing extremely convenient channels for electron transfer and the migration of active species during the reaction process.

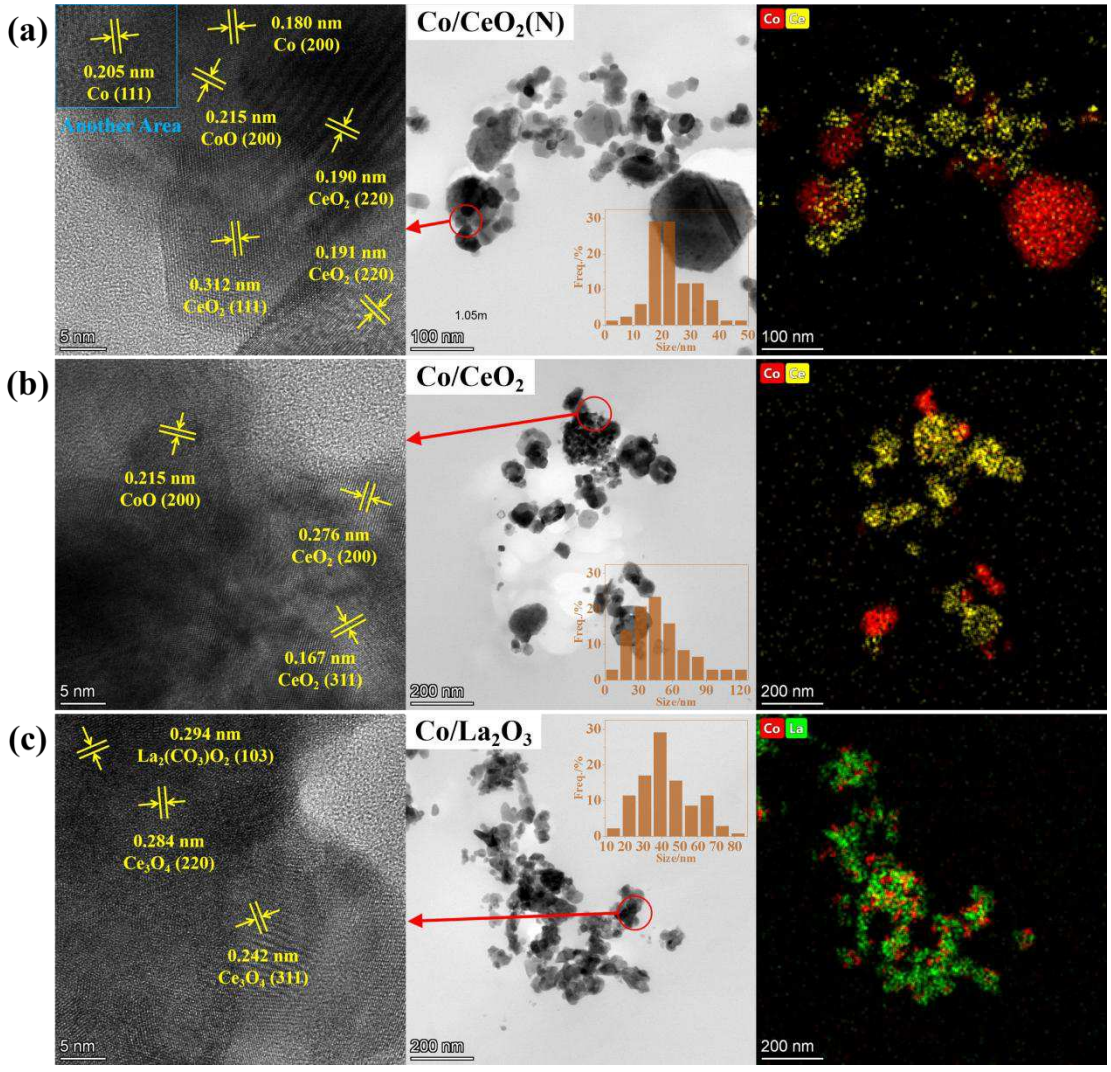


Fig.8 HRTEM (left), TEM (middle), and EDS elemental mapping (right) images of representative catalysts: (a) $Co/CeO_2(N)$; (b) Co/CeO_2; (c) Co/La_2O_3.

In contrast, the Co/CeO_2 sample with a micrometer-sized cerium oxide as the carrier (Figure 3-6(b)) exhibited distinct morphological characteristics. The TEM images showed that the particle size of the carrier was significantly increased, even in the more dispersed areas, and was much larger than

that of the $Co/CeO_2(N)$ sample. In the area shown in the picture, the main form was spherical polyhedra with a particle size of approximately 40 nm, while from the overall morphology, it was mainly large elliptical block-like structures with a size of around 200 nm. Although the cobalt species still maintained a certain degree of dispersion on the carrier surface, compared to the $Co/CeO_2(N)$ sample, the metal particles underwent significant agglomeration, and the average particle size significantly increased. This agglomeration effect led to a decrease in the distribution density of the active components on the carrier surface, and obvious voids appeared in local areas. This was a reasonable geometric explanation for why its catalytic activity was slightly inferior to the nano-carrier system. The larger metal particle size not only reduced the specific surface area but also directly decreased the total number of effective active sites exposed per unit mass of the catalyst [62].

For the Co/La_2O_3 sample (Figure 3-6(c)), the EDS spectrum confirmed the extremely high dispersion of cobalt elements, which was superior to Co/CeO_2 and even showed a dispersion trend exceeding that of $Co/CeO_2(N)$ in some areas, which also explained why Co/La_2O_3 also had excellent performance second only to $Co/CeO_2(N)$. At the same time, the HRTEM image on the left revealed its unique steady-state mechanism. It can be observed that the lattice stripes of the metal cobalt are often tightly encapsulated by a layer of amorphous or low crystallinity on the carrier surface (possibly due to the carbonation of La_2O_3 on the surface). This special embedding structure is not merely a physical barrier but an effective spatial confinement mechanism that restricts the migration and agglomeration of cobalt nanoparticles at high temperatures, significantly enhancing the catalyst's resistance to sintering.

In conclusion, the microscopic morphology characterization further confirmed the core viewpoint of this study, that is, in the design of ammonia decomposition catalysts, the chemical interaction between the carrier and the active metal (SMSI) contributes more to the catalytic performance than the influence of the physical specific surface area. The CeO_2 and La_2O_3 carriers achieved efficient utilization of cobalt through this chemical regulation mechanism, overcoming the limitations of physical texture.

3.5 Surface Chemical Properties of the Catalysts

3.5.1 Analysis of Surface Element Valence States

To deeply explore the regulatory mechanism of carrier properties on the electronic state and reduction behavior of the active component, X-ray photoelectron spectroscopy (XPS) was used to

characterize the samples after reduction and air passivation. Figure 9 shows the XPS spectra of Co2p for different carrier catalyst samples and their peak fitting results.

Looking at the spectra of the eight samples as a whole, all catalysts show clear $Co2p_{3/2}$ and $Co2p_{1/2}$ spin-orbit splitting peaks in the binding energy range of 778 - 782 eV and 793 - 797 eV, and the high binding energy side is accompanied by satellite peaks (Satellite peaks). According to the strength of the satellite peaks, the oxides of cobalt on CeO_2 and La_2O_3 carriers mainly exist in the form of Co_3O_4, while on the other carriers, it is mainly CoO. Considering that cobalt was not reduced, it is speculated that extremely stable structures such as cobalt aluminum oxide (CoAl2O4) spinels and Co-Mg-O solid solutions were formed, which not only prevented cobalt from being reduced to the active metal phase but also led to a lack of electron feedback mechanism on the surface, thereby reducing the catalytic activity.

The fitting results show that compared with the standard metal cobalt's Co0 at 778.2 eV and Coδ+ at 779.7 eV, all loaded catalysts show different degrees of blue shift (red shift) of the Co characteristic peaks. This widespread blue shift phenomenon is mainly attributed to the "small size effect" of the nano-sized cobalt particles, that is, when the metal particles are reduced to the nanoscale (especially < 10 nm), the electrons outside the nucleus are more strongly bound by the atomic nucleus, resulting in a decrease in the kinetic energy of photoelectrons and an increase in binding energy [63].

The $Co/Al_2O_3(N)$ sample shows a large binding energy shift (approximately 1.0 eV). This excessive blue shift indicates that in addition to the small size effect, there is a strong electron extraction effect between the acidic alumina carrier and the cobalt species (or a surface phase with a deficient electron state of cobalt aluminate is formed), causing the active center to be in an extremely "electron-poor" state. Although this strong Lewis acidity is beneficial for the adsorption of ammonia molecules, it also has an overly strong attraction effect on the nitrogen atom of the reaction intermediate product. The extremely strong Co-N bond strength significantly increases the energy barrier for the recombination and desorption of the nitrogen atom on the catalyst surface, which is not conducive to the forward reaction, and this may be one of the reasons for the poor performance of $Co/Al_2O_3(N)$.

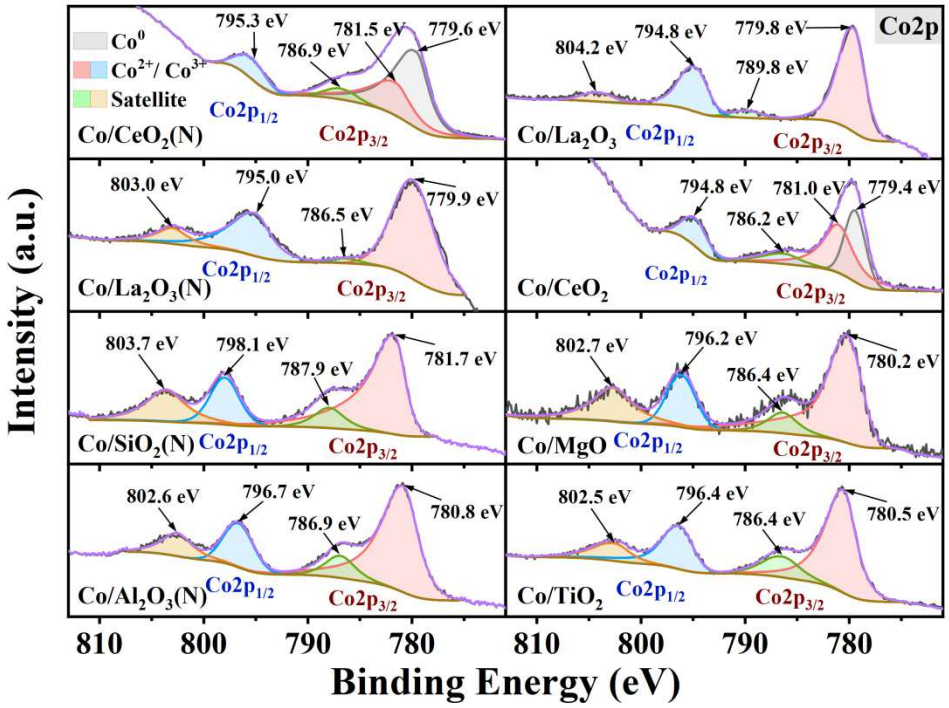


Fig.9 Co2p XPS spectra of catalysts supported on different carriers

In contrast, the blue shift of the $Co/CeO_2(N)$ and Co/La_2O_3 samples with rare earth carriers is relatively small (with moderate binding energy). This indicates that the unique electron-donating properties of the carriers, such as the oxygen vacancies in CeO_2 or the basicity of La_2O_3, compensate for the electron loss caused by the small size effect to some extent, maintaining the active cobalt sites in a moderately electron-deficient state [64]. This electronic structure ensures that sufficient electrophilicity is retained to effectively adsorb ammonia molecules while the relatively low positive charge density avoids excessive adsorption of N atoms, ensuring that the Co-N bond has an appropriate strength, allowing the product N_2 to be smoothly desorbed from the surface [65].

In the comparison of the Co2p spectra of all catalysts, only the spectra of $Co/CeO_2(N)$ and Co/CeO_2 samples show clear identifiable metal cobalt (Co0) characteristic peaks, which may be attributed to the unique "reducing aid" property of the CeO_2 carrier. The CeO_2 lattice contains rapid conversions of Ce3+ and Ce4+, enabling it to easily activate hydrogen molecules. During the reduction process, the dissociated active hydrogen species (H*) adsorbed on the CeO_2 surface or interface can rapidly migrate to the adjacent cobalt oxide species through the overflow effect [66]. This active hydrogen has extremely high reactivity and can effectively break the Co-O bond, thereby promoting the deep transformation of cobalt oxide to metal cobalt under relatively mild conditions. Therefore, the

significant Co0 signal in XPS confirms that the CeO_2 carrier successfully assisted the generation of the active phase, exposing a large number of intrinsic metal active sites.

To further reveal the structural origin of the Co2p binding energy shift and the strong metal-carrier interaction, the XPS spectra of O1s for each catalyst were analyzed in detail. Figure 10 shows the O1s spectra of different carrier catalyst samples and their peak fitting results. Different carriers exhibit distinct oxygen species distribution characteristics.

According to the chemical properties of the oxide surface, the O1s spectra are usually fitted with three characteristic peaks, corresponding to different chemical environments. The lattice oxygen (Oα) is located at the lower binding energy (approximately 529 - 530 eV), belonging to the O^{2-} in the metal oxide lattice; the surface adsorbed oxygen or defect oxygen (Oβ) is located at the intermediate binding energy (approximately 531 - 532 eV), corresponding to the active oxygen species (such as O−, O_2^{2-}) adsorbed by oxygen vacancies or low-coordination oxygen, and the relative content of this species is a key indicator for measuring the surface defect concentration of the carrier; the surface hydroxyl or adsorbed water (Oγ) is located at the higher binding energy (> 532.0 eV), usually belonging to the water molecules or hydroxyl species physically adsorbed on the surface.

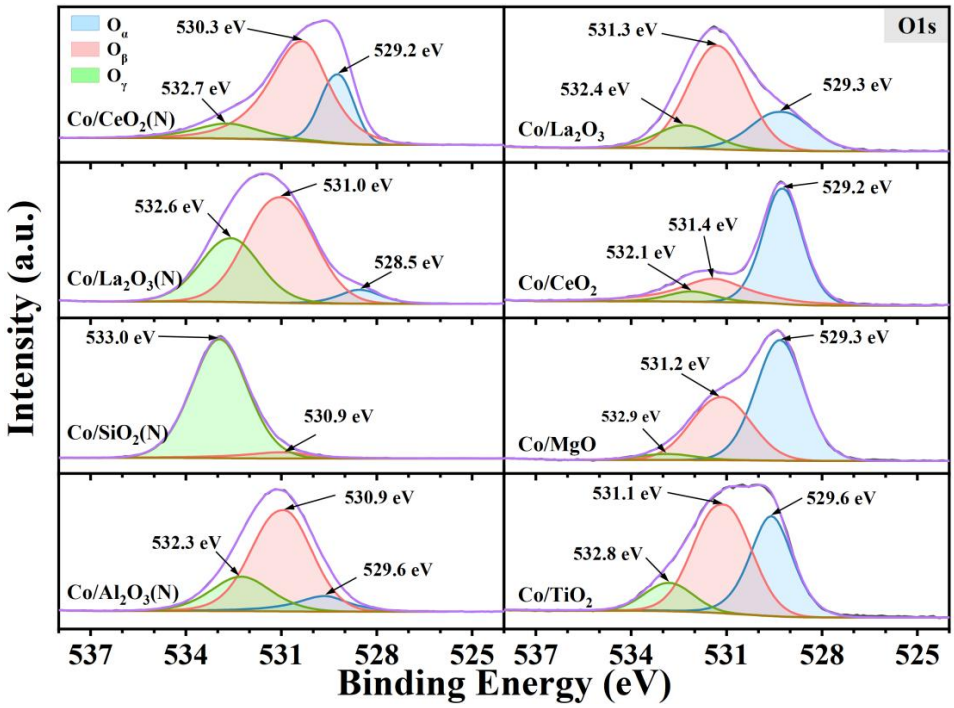


Fig.10 O1s XPS spectra of catalysts supported on different carriers

In the spectrum of Co/CeO_2(N), the lattice oxygen peak (Oα) at 529.2 eV and the defect oxygen

peak (Oβ) at 530.3 eV can be clearly distinguished. The Oβ peak has a significant area, and its relative content (Oβ / Ototal) ranks at the top among all samples. This feature directly confirms the existence of extremely high concentrations of oxygen vacancies on the surface of nano-CeO_2. In the catalytic system, these abundant oxygen vacancies not only act as electronic regulation hubs, effectively regulating the electronic state of cobalt species through strong metal-oxide interaction, but also serve as cooperative active sites, assisting in the adsorption and activation of ammonia molecules, especially promoting the dehydrogenation process of intermediate species (NHx).

The lattice oxygen binding energy of Co/La_2O_3(N) sample is the lowest (528.5 eV), reflecting the strong ionic nature of La-O bonds and the strong Lewis basicity of the carrier. The Oβ peak (531.0 eV) is also prominent, which may be related to the formation of $La_2(CO_3)O_2$ on the surface or surface defects. These acidic sites also facilitate the feedback of electrons to the metal cobalt.

The main peak of Co/Al_2O_3(N) is located at a higher binding energy (530.9 eV), which usually belongs to the lattice oxygen of Al-O bonds. It is prone to overlap with the defect oxygen peak, making it difficult to distinguish. Similarly, Co/SiO_2(N) mainly shows a broad and symmetrical main peak at a higher binding energy of 533.0 eV. This characteristic peak belongs to the strong covalent Si-O-Si bond in the silica framework and is classified as lattice oxygen. This high binding energy reflects the extremely strong electron binding ability and chemical stability of Si-O bonds. The lack of low-binding-energy lattice oxygen peaks and characteristic defect oxygen shoulder peaks in the spectrum indicates that the SiO_2 surface is difficult to form active oxygen vacancies or participate in the exchange cycle of oxygen species like CeO_2.

Furthermore, comparing different scale carriers, it is found that on the whole, the micrometer-scale carriers exhibit sharp and intense lattice oxygen peaks (Oα), while the lattice oxygen signals of the nanometer-scale carriers are significantly weakened, and the proportion of defect oxygen (Oβ) increases relatively. This phenomenon is mainly attributed to the extremely high surface/phase atomic ratio of nanomaterials. Due to the detection depth of XPS being only a few nanometers from the surface, the signals mainly reflect the highly exposed surface coordination unsaturation state and defect structure of the nanoparticles, rather than the regular crystal lattice inside.

In conclusion, XPS analysis confirms that the excellent catalytic performance of Co/CeO_2(N) is attributed to its oxygen vacancy-induced electronic regulation mechanism. The high concentration of oxygen vacancies on the carrier surface induces strong metal-oxide electronic interaction, causing the

active metal cobalt to be in a moderately electron-rich and highly reduced state, thereby significantly reducing the activation energy of the rate-determining step of the ammonia decomposition reaction.

3.5.2 Reduction property analysis

To explore the true existence state of the catalyst after reduction treatment and the reversibility of the surface species' oxidation-reduction, H_2-TPR characterization was performed on the catalyst reduced at 550℃ in ammonia atmosphere and then passivated by air. Figure 11 shows the hydrogen consumption profiles of each sample.

It should be noted that since the samples have been pre-reduced at high temperatures, theoretically the phase has been transformed into metal cobalt. Therefore, the low-temperature hydrogen consumption peaks in the spectrum mainly belong to the re-reduction of the surface oxide passivation layer, while the high-temperature peaks correspond to the residual refractory species or the carrier itself that have not been reduced during the pre-treatment.

Co/CeO_2(N) shows a unique and sharp hydrogen consumption peak in the low-temperature region (256℃). This temperature is significantly lower than that of other carrier systems, indicating that the oxide passivation layer formed on the surface of Co/CeO_2 is extremely unstable and can easily be reconverted into active metal cobalt through hydrogen treatment. This remarkable "low-temperature regeneration ability" is attributed to the abundant oxygen vacancies on the surface of nano-CeO_2 and the hydrogen overflow effect. Even if the surface is oxidized, it can be rapidly reduced and activated in the initial stage of the reaction. Moreover, this sample shows no significant hydrogen consumption in the high-temperature zone, confirming that the ammonia pre-treatment at 550℃ has successfully reduced the majority of the Co species to the metallic state, and there are no remaining refractory phases that are difficult to reduce.

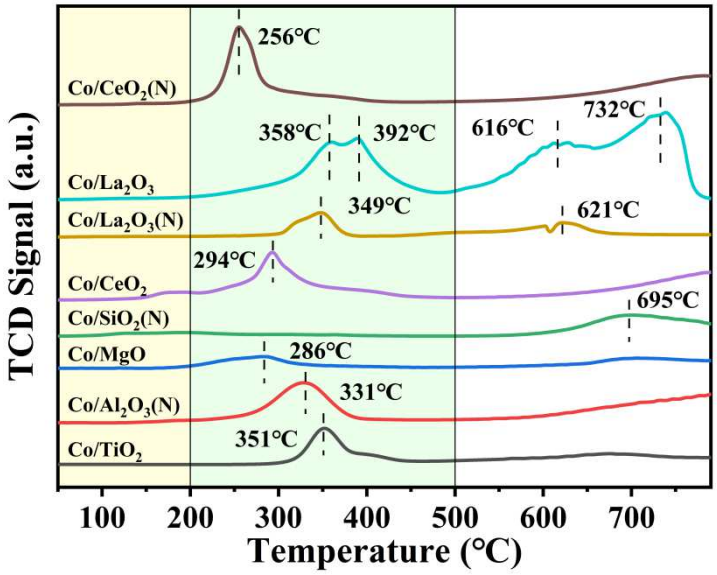


Fig.11 H_2-TPR profiles of catalysts supported on different carriers

In contrast, the reduction peak of the passivation layer of $Co/Al_2O_3(N)$ was delayed to 331°C, and the peak width was relatively large. This indicates that on the surface of alumina, the interaction between the Co species and the carrier is stronger, and the formed surface oxide layer is more difficult to be removed. The reduction behavior of Co/TiO_2 is similar, with the peak temperature located at 351°C. This means that during the initial stage of the actual reaction, these catalysts require a higher temperature or a longer time to completely activate the surface active sites.

$Co/SiO_2(N)$ exhibits completely different characteristics. It shows almost no obvious hydrogen consumption signal in the low-temperature range, indicating that either its surface is difficult to form a passivation layer or the passivation layer is extremely thin. However, a strong hydrogen consumption peak appears at 695°C. This strongly suggests that during the ammonia pre-treatment at 550°C, there are still a large number of cobalt species (possibly cobalt silicate, CO_2SiO4) that have not been reduced. These residual oxidized species need to be reduced at temperatures close to 700°C in TPR, which explains why this sample performs poorly in the low-temperature segment of the activity test, but significantly improves after 600°C - because the effective metal active sites are severely lacking and are only exposed after being reduced at high temperatures.

The spectrum of Co/La_2O_3 is the most complex. In addition to the surface cobalt species reduction peaks at 358°C and 392°C, there are huge broadened hydrogen consumption bands at 616°C and 732°C. Given that the sample has been pre-reduced, these high-temperature signals mainly belong to the

783 decomposition and reduction of $La_2(CO_3)O_2$ formed by the carrier during ammonia treatment or air
784 contact. This further confirms the structural sensitivity of the lanthanum-based carrier in the reaction
785 environment.

786 The H_2-TPR results reveal the essential differences in the surface species of the pre-reduced
787 catalysts. $Co/CeO_2(N)$ demonstrates the lowest re-reduction temperature (256℃) and the absence of
788 residual refractory phases, proving that not only is its reduction degree high, but also the surface metal
789 sites are extremely easy to maintain an active state in the reaction atmosphere. In contrast, carriers such
790 as $Co/SiO_2(N)$ have a large number of residual species that are difficult to be reduced at 550℃, limiting
791 their catalytic performance in the low-temperature segment.

792 3.5.3 Surface Basic Sites Analysis

793 In addition to the redox properties, the acid-base properties of the carrier surface also have a
794 decisive influence on the ammonia decomposition reaction process. Since ammonia molecules are
795 Lewis bases, and the reaction's rate-determining step usually involves the breaking of the N-H bond
796 (requiring electron injection into the antibonding orbital), the basic sites (Basic Sites) on the carrier
797 surface are generally considered to be able to promote the activation of the metal by electron-induced
798 effects.

799 To evaluate the strength and distribution of the basic sites on the catalyst surface, CO_2-TPD
800 characterization was performed on the reduced samples. Figure 12 shows the CO_2 desorption spectra of
801 each catalyst. Generally, the basic sites are classified by desorption temperature into three categories:
802 weak basic sites (< 200℃, corresponding to surface hydroxyl groups or physical adsorption),
803 moderately strong basic sites (200-500℃, corresponding to M-O or M-O-M pairs), and strong basic
804 sites (> 500℃, corresponding to low-coordinated lattice oxygen).

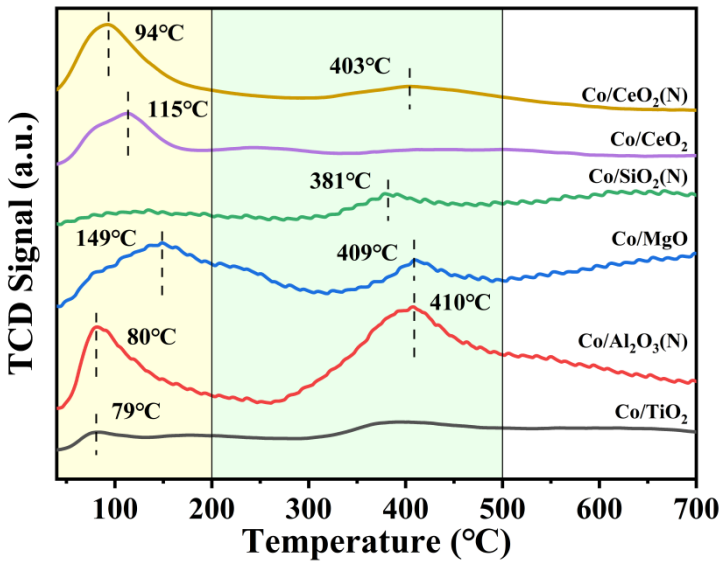


Fig.12 CO_2-TPD profiles of catalysts supported on different carriers

As shown in Figure 12, the $Co/CeO_2(N)$ with the best activity exhibited the widest and most significant desorption characteristics. A sharp desorption peak appeared at the low-temperature region of 94°C, indicating the presence of abundant weakly basic sites. More importantly, it showed a huge broadening desorption band in the wide range of 200–500°C, with the center located at approximately 403°C. The basic sites in this region are usually closely related to surface oxygen vacancies. Combined with the previous O1s XPS results, it can be confirmed that the high concentration of oxygen vacancies on the nano-sized cerium oxide surface acts as a Lewis basic center. During the reaction process, these sites not only enhance the electron density of nitrogen atoms, promoting the breakage of N-H bonds, but also inhibit the strong adsorption of acidic sites on the product H_2, avoiding hydrogen poisoning, and thus demonstrating excellent catalytic activity. In contrast, the signal of Co/CeO_2 in the same region is extremely weak, again confirming the amplification effect of the nano-scale on the alkalinity of surface defects.

For the Co/La_2O_3 sample, in order to avoid its extremely high intensity signal masking the characteristics of other samples, the curve of this sample was excluded in Figure 12. This sample showed an extremely large CO_2 desorption peak in the high-temperature region (about 734°C), with the peak intensity being approximately 12 times that of the main peak of $Co/CeO_2(N)$. Such a huge desorption amount and extremely high desorption temperature reveal the unique chemical properties of this carrier, which exceeds the scope of conventional surface strong basic sites and essentially

corresponds to the decomposition of thermodynamically extremely stable phase $La_2(CO_3)O_2$ species. This result quantitatively confirms that La_2O_3 has a very strong capture ability for acidic molecules and an extremely high alkaline strength. Although this extremely strong alkalinity is theoretically very conducive to feedback of electrons to the active metal, in the actual reaction environment, the carrier is prone to over-absorb the reaction products or impurities, forming a thick carbonate coating (which is consistent with the "embedded" structure observed in TEM), thereby to some extent, forming physical steric hindrance, limiting the contact between reactants and internal metal active sites. This also reasonably explains why its alkalinity is far greater than cerium oxide, but the final catalytic activity is second.

$Co/Al_2O_3(N)$ shows a double-peak characteristic at 80℃ (weak base) and 410℃ (medium-strong base). Although it also has some medium-strong basicity, considering the amphoterically acidic nature of alumina itself, its electron donor ability is much weaker than that of rare earth oxides, and it is difficult to effectively control the electronic state of cobalt. $Co/SiO_2(N)$ has a weak signal only at 381℃, indicating that its surface is chemically inert and lacks effective basic sites to activate reaction molecules. Co/MgO, as a typical alkaline earth metal oxide, shows a clear broad peak at 149℃ and 409℃, indicating good surface alkalinity. However, due to its formation of a difficult-to-reduce solid solution (Co-Mg-O), even with an alkaline surface, it cannot compensate for the deficiency of metal active sites.

In conclusion, CO_2-TPD reveals the characteristics of alkaline sites for catalytic activity, and $Co/CeO_2(N)$ has the optimized distribution of medium-strong basic sites. This moderate alkalinity dominated by oxygen vacancies can provide sufficient electrons to activate N-H bonds, and does not cause surface poisoning or reconstruction like La_2O_3 due to excessive alkalinity, thus achieving the optimization of catalytic performance.

3.6 Effect of Space Velocity on Catalytic Performance

To explore the external mass transfer diffusion limitation and determine the optimal operating window of the catalyst, the influence of mass velocity (WHSV) on the ammonia decomposition performance of the optimal $Co/CeO_2(N)$ catalyst at different reaction temperatures (550℃, 600℃, 650℃) was investigated. The test range was set at 2,000 - 15,000 mL/(h·g_{cat}). The results are shown in Figure 13.

From the figure, it can be observed that at a higher reaction temperature (650℃), the ammonia

decomposition conversion rate shows extreme insensitivity to changes in space velocity. Even when the space velocity increased from 2,000 to 15,000 mL/(h·g_{cat}), the ammonia conversion rate remained above 99.2% at all times, almost maintaining a horizontal line. This indicates that at this high-temperature condition, the catalyst has extremely high intrinsic activity and a very fast reaction rate, and the reaction system may be close to the thermodynamic equilibrium state. At this point, increasing the gas flow rate is not sufficient to change the macroscopic conversion rate.

In contrast, at a relatively lower temperature (550°C), the catalytic activity shows significant speed dependence. As the WHSV increased from 2,000 to 15,000 mL/(h·g_{cat}), the ammonia conversion rate showed a significant downward trend, dropping from approximately 94% to around 81%, but the rate of decline slowed down as the space velocity increased. This phenomenon is mainly attributed to the shortening of the contact time. In the low-temperature kinetic control region, the adsorption-surface reaction-desorption process of ammonia molecules at the active sites is the rate-determining step. As the space velocity increases, the residence time of reactant molecules in the catalyst bed layer significantly decreases, resulting in some ammonia molecules not having the opportunity to undergo dissociation reactions at the active sites before flowing out of the reactor, thereby causing a decrease in the macroscopic conversion rate.

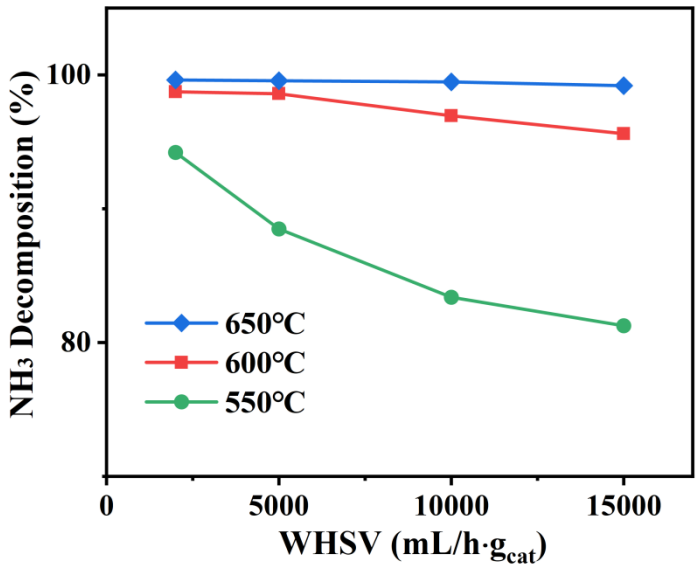


Fig.13 Effect of WHSV on the catalytic performance of Co/CeO_2(N) at different reaction temperatures

At 600°C, the catalyst exhibited a transitional behavior between the two extremes. At low space velocities (< 5,000 mL/(h·g_{cat})), the conversion rate was close to 100%; however, as the space velocity

increased further, the conversion rate began to decline slowly, indicating that the system gradually shifted from equilibrium control to kinetic control.

In summary, the Co/CeO_2(N) catalyst maintained relatively good catalytic activity over a wide range of space velocities. Particularly at 550°C, the conversion rate varied significantly with the space velocity, indicating that this condition was in the kinetic sensitive zone, which could most accurately reflect the intrinsic activity differences of the catalyst.

3.7 Stability Evaluation

The catalyst's resistance to deactivation (i.e., stability) is a key indicator for assessing its potential for industrial application [67, 68]. To more rigorously evaluate the stability of the catalyst, the Co/CeO_2(N) catalyst with the best overall performance was selected. It was subjected to a continuous online durability test for 50 hours at 550°C and WHSV = 2,000 mL/(h·g_{cat}) to ensure the sensitive monitoring of possible deactivation phenomena under non-100% conversion rates. The test results are shown in Figure 14.

Figure 14 uses a dual Y-axis coordinate system to present the test results. The left Y-axis (corresponding to the blue curve) represents the real-time ammonia conversion rate recorded every 30 minutes. From the figure, it can be seen that during the entire 50-hour test period, the blue data points almost formed a straight line, with the conversion rate consistently maintaining a high level above 93%, without any obvious monotonic decline trend.

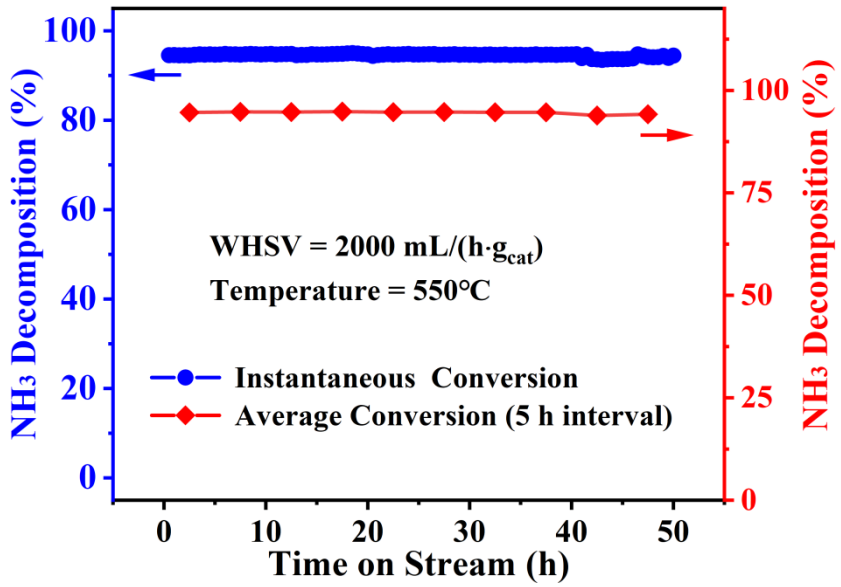


Fig.14 Stability test of the Co/CeO_2(N) catalyst at 550°C

The right Y-axis (corresponding to the red curve) represents the average ammonia conversion rate calculated every 5 hours. It should be noted that although the red line graph visually shows some oscillation, this is mainly due to the extremely large scale range of the right coordinate axis (only covering the narrow interval of 90% - 97%). In fact, the maximum fluctuation of the catalyst activity is less than 1.0%. This extremely small fluctuation is within the normal disturbance range allowed by the experiment and not a sign of catalyst deactivation.

$Co/CeO_2(N)$ exhibits remarkable stability, which is closely related to its unique microstructure. Combined with the TEM characterization in the previous text, the strong metal-载体 interaction between the nano-sized cerium oxide carrier and the cobalt species plays a crucial anchoring role. This interaction effectively inhibits the migration and agglomeration of metal cobalt particles during the high-temperature (550℃) reaction process, thus maintaining a high density of active sites. Moreover, the excellent oxygen storage and release ability of CeO_2 helps to promptly eliminate trace nitrogen-containing substances or carbon precursor deposits on the active sites, maintaining the cleanliness of the surface.

Therefore, the durability test results confirm that the $Co/CeO_2(N)$ catalyst not only has excellent medium and low-temperature activity, but also possesses excellent structural stability and anti-sintering ability, capable of meeting the requirements of long-term continuous operation, and demonstrating a favorable industrial application prospect.

4. Summary

This chapter aims to develop an efficient non-precious metal ammonia decomposition catalyst. It systematically investigated various oxide carriers (Co/CeO_2, Co/La_2O_3, Co/SiO_2, Co/MgO, Co/Al_2O_3, Co/TiO_2, etc.) and their microscale (nano, micrometer) regulation laws on the performance of cobalt-based catalysts. Combined with multi-dimensional physical and chemical characterization, it deeply clarified the structure-activity relationship between the carrier properties and catalytic activity. The main conclusions are as follows：

(1) The activity test results show that the physical and chemical properties of the carrier play a dominant role in catalytic efficiency. $Co/CeO_2(N)$ exhibits the most excellent medium and low-temperature catalytic activity (T100 ≈ 550℃), and its performance is significantly better than that of micrometer-sized similar carriers and other oxide systems. Co/La_2O_3 demonstrates activity second

only to the cerium-based catalyst due to its unique surface properties, while $Co/Al_2O_3(N)$, with the largest specific surface area, performs poorly due to the low intrinsic activity of the active sites. This strongly proves that in the ammonia decomposition reaction, the chemical interaction between the carrier and the metal is more crucial than the simple physical surface area.

(2) XPS and H_2-TPR characterization revealed the physical and chemical essence of the performance differences. The nano-sized CeO_2 carrier achieved deep reduction of the active component at low temperatures (reduction peak temperature as low as 256℃) and the stable existence of the metal state (Co0). More importantly, the carrier imposed a moderate electron regulation (Co2p binding energy slightly increased) on the metal cobalt, keeping the active centers at the optimal electron energy level for adsorption-desorption balance. This moderate electron deficiency state not only ensures effective adsorption of reactants NH_3 but also avoids excessive binding of intermediate product N atoms, effectively overcoming the "nitrogen poisoning" phenomenon. In contrast, the extremely poor electron state induced by acidic carriers (significant increase) leads to difficulties in N atom desorption and the formation of difficult-to-reduce spinel phase on the surface, limiting the number of effective active sites.

(3) CO_2-TPD confirmed that $Co/CeO_2(N)$ has abundant and uniformly distributed medium-strong basic sites (corresponding to surface oxygen vacancies), which can effectively assist the activation of N-H bonds by the active metal. Although Co/La_2O_3 exhibits extremely strong surface alkalinity (owing to calcium oxide lanthanum), which is conducive to electron feedback, XRD and TEM reveal that its surface is prone to form a thick carbonate coating. This "encapsulation" structure not only inhibits metal sintering but also causes physical steric hindrance, limiting the further release of its activity.

(4) At 550℃ and higher gas flow rates, $Co/CeO_2(N)$ withstood a continuous stability test for 50 hours, with the ammonia conversion rate remaining above 93% throughout, and no obvious deactivation was observed. This is attributed to the strong anchoring effect provided by the strong metal-support interaction effect, effectively inhibiting the migration and agglomeration of active particles at high temperatures.

In conclusion, $Co/CeO_2(N)$ with its easily reducible highly dispersed metal center, moderately regulated electronic structure, and abundant medium-strong alkalinity induced by oxygen vacancies, combines the advantages of a single metal cobalt-based supported catalyst that overcomes the limitation of physical surface area and becomes the optimal catalyst selected in this chapter's research.

Notes

The authors declare no competing financial interest.

Data availability

The data that support the findings of this study are available on request.

Acknowledgement

This work was Sponsored by the National Natural Science Foundation of China (52476124, U2572206, 52076134, 51676127, 51436005, and 51176118), the National Key Research and Development Plan (2016YFC0205200, 2016YFC0208000, and 2017YFB0103501), the High-tech Ship Research Projects “Key combustion technology research for ammonia-fueled marine engines based on the Otto cycle”, the Oceanic Interdisciplinary Program of Shanghai Jiao Tong University (SL2022MS006), Major Science and Technology Projects of Yunnan Province (202402AC080004), the Open Research Program of State Key Laboratory of Engines (K2023-06), Scientific and Technological Project of Yunnan Precious Metals Laboratory (YPML-20240502068), Systematic Technical Research on Hybrid-Specific Gasoline Engines for CN7 Emission Standards (20240301004ZD), the National Engineering Laboratory for Mobile Source Emission Control Technology (NELMS2017A07), the National Natural Science Foundation of China for Young Scientists (51306115), the Low Speed Marine Engine Project (CDGC01-KT1203), and the Scientific Research Foundation for the Returned Overseas Chinese Scholars of State Education Ministry.

References

[1] Gielen, D., F. Boshell, D. Saygin, M.D. Bazilian, N. Wagner, and R. Gorini, The role of renewable energy in the global energy transformation, Energy Strategy Reviews 24 (2019) 38-50.

[2] Yang, L., S. Wang, Z. Zhang, K. Lin, and M. Zheng, Current development status, policy support and promotion path of China's green hydrogen industries under the target of carbon emission peaking and carbon neutrality, Sustainability 15 (2023) 10118.

[3] Bouckaert, S., A.F. Pales, C. McGlade, U. Remme, B. Wanner, L. Varro, D. D'Ambrosio, and T. Spencer, Net zero by 2050: A roadmap for the global energy sector, (2021).

[4] Yue, M., H. Lambert, E. Pahon, R. Roche, S. Jemei, and D. Hissel, Hydrogen energy systems: A critical review of technologies, applications, trends and challenges, Renewable and Sustainable Energy Reviews 146 (2021) 111180.

[5] Li, J., M.S. Ho, C. Xie, and N. Stern, China's flexibility challenge in achieving carbon neutrality by 2060, Renewable and Sustainable Energy Reviews 158 (2022) 112112.

[6] Allendorf, M.D., V. Stavila, J.L. Snider, M. Witman, M.E. Bowden, K. Brooks, B.L. Tran, and T. Autrey, Challenges to developing materials for the transport and storage of hydrogen, Nature Chemistry 14 (2022) 1214-1223.

[7] Ma, N., W. Zhao, W. Wang, X. Li, and H. Zhou, Large scale of green hydrogen storage: Opportunities and challenges, International Journal of Hydrogen Energy 50 (2024) 379-396.

[8] Mekonnin, A.S., K. Wacławiak, M. Humayun, S. Zhang, and H. Ullah, Hydrogen storage technology, and its challenges: a review, Catalysts 15 (2025) 260.

[9] Ghorbani, B., S. Zendehboudi, N.M.C. Saady, X. Duan, and T.M. Albayati, Strategies To Improve the Performance of Hydrogen Storage Systems by Liquefaction Methods: A Comprehensive Review, ACS Omega 8 (2023) 18358-18399.

[10] Naquash, A., N. Agarwal, and M. Lee, A review on liquid hydrogen storage: current status, challenges and future directions, Sustainability 16 (2024) 8270.

[11] Wen, Z., B. Huang, Y. Wang, K. Wang, X. Tu, P. Xie, and X. Fu, Ammonia as a renewable energy carrier from synthesis to utilization, Nature Reviews Clean Technology 1 (2025) 755-770.

[12] Aziz, M., A.T. Wijayanta, and A.B.D. Nandiyanto, Ammonia as effective hydrogen storage: A review on production, storage and utilization, Energies 13 (2020) 3062.

[13] Serpell, O., Z. Hsain, A. Chu, and W. Johnsen, Ammonia's role in a net-zero hydrogen economy, Kleinman Center for Energy Policy 17 (2023).

[14] Jiang, L. and X. Fu, An Ammonia–Hydrogen Energy Roadmap for Carbon Neutrality: Opportunity and Challenges in China, Engineering 7 (2021) 1688-1691.

[15] Lucentini, I., X. Garcia, X. Vendrell, and J. Llorca, Review of the Decomposition of Ammonia to Generate Hydrogen, Industrial & Engineering Chemistry Research 60 (2021) 18560-18611.

[16] Zhao, Z., W. He, B. Guo, J. Yu, Z. Wang, and H. Yu, A Comprehensive Review of Ammonia Decomposition for Hydrogen Production, Energy & Fuels 39 (2025) 13825-13847.

[17] Ganley, J.C., F. Thomas, E. Seebauer, and R.I. Masel, A priori catalytic activity correlations: the difficult case of hydrogen production from ammonia, Catalysis Letters 96 (2004) 117-122.

[18] Zhang, J., J. Le, Y. Dong, L. Bu, Y. Zhang, J. Cheng, L. Li, and X. Huang, Face-centered cubic structured RuCu hollow urchin-like nanospheres enable remarkable hydrogen evolution catalysis, Science China Chemistry 65 (2022) 87-95.

[19] Zhou, C., K. Wu, H. Huang, C.-F. Cao, Y. Luo, C.-Q. Chen, L. Lin, C. Au, and L. Jiang, Spatial confinement of electron-rich Ni nanoparticles for efficient ammonia decomposition to hydrogen production, Acs Catalysis 11 (2021) 10345-10350.

[20] Liu, H., Y. Zhang, S. Liu, S. Li, and G. Liu, Ni-CeO2 nanocomposite with enhanced metal-support interaction for effective ammonia decomposition to hydrogen, Chemical Engineering Journal 473 (2023) 145371.

[21] Xu, Y.-S., W.-W. Wang, K. Xu, X.-P. Fu, and C.-J. Jia, Multicomponent Ni–Y2O3–Al2O3 nanospheres as highly efficient catalysts for the ammonia decomposition reaction, ACS Applied Nano Materials 6 (2023) 19300-19311.

[22] Pinzón, M., A. Sánchez-Sánchez, A. Romero, A. De la Osa, and P. Sánchez, Self-combustion Ni and Co-based perovskites as catalyst precursors for ammonia decomposition. Effect of Ce and Mg doping, Fuel 323 (2022) 124384.

[23] Han, X., M. Hu, J. Yu, X. Xu, P. Jing, B. Liu, R. Gao, and J. Zhang, Dual confinement of LaCoOx modified Co nanoparticles for superior and stable ammonia decomposition, Applied Catalysis B: Environmental 328 (2023) 122534.

[24] Bell, T.E. and L. Torrente-Murciano, H2 production via ammonia decomposition using non-noble metal catalysts: a review, Topics in Catalysis 59 (2016) 1438-1457.

[25] Qi, X., Y. Zhang, C. Chen, J. Yang, J. Wen, Z. Zhuang, Z. Zhang, D. Wang, and H. Zhang, Deciphering the N─N Coupling Mechanism Over Iron–Copper Alloy Catalysts During Ammonia Decomposition, Angewandte Chemie International Edition 64 (2025) e202509322.

[26] Yuan, Y., W. Wang, D. Li, R. Hu, A. Yan, and Z. Wang, Highly efficient and stable non-noble metal CoM@NC (M = Ni, Mo) catalysts for NH3 decomposition, Molecular Catalysis 572 (2025) 114800.

[27] Li, J., B. Sheng, Y. Chen, J. Yang, P. Wang, Y. Li, T. Yu, H. Pan, L. Qiu, Y. Li, J. Song, L. Zhu, X. Wang, Z. Huang, and B. Zhou, Utilizing full-spectrum sunlight for ammonia decomposition to hydrogen over GaN nanowires-supported Ru nanoparticles on silicon, Nature Communications 15 (2024) 7393.

[28] Chen, R., H. Pan, Z. Meng, H. Tang, Q. Li, T. Tian, X. Huang, Z. Zhan, and H. Tang, Electronic structure optimizing of Ru nanoparticles loaded on carbon via amorphous Pr2O3 for accelerating hydrogen production from ammonia decomposition, Advanced Composites and Hybrid Materials 8 (2025) 164.

[29] Ganley, J.C., F.S. Thomas, E.G. Seebauer, and R.I. Masel, A Priori Catalytic Activity Correlations: The Difficult Case of Hydrogen Production from Ammonia, Catalysis Letters 96 (2004) 117-122.

[30] Boisen, A., S. Dahl, J.K. Nørskov, and C.H. Christensen, Why the optimal ammonia synthesis catalyst is not the optimal ammonia decomposition catalyst, Journal of Catalysis 230 (2005) 309-312.

[31] Hansgen, D.A., D.G. Vlachos, and J.G. Chen, Using first principles to predict bimetallic catalysts for the ammonia decomposition reaction, Nature Chemistry 2 (2010) 484-489.

[32] Su, T., B. Guan, J. Zhou, C. Zheng, J. Guo, J. Chen, Y. Zhang, Y. Yuan, W. Xie, N. Zhou, H. Dang, B. Xu, and Z. Huang, Review on Ru-Based and Ni-Based Catalysts for Ammonia

Decomposition: Research Status, Reaction Mechanism, and Perspectives, Energy & Fuels 37 (2023) 8099-8127.

[33] García-García, F., A. Guerrero-Ruiz, and I. Rodríguez-Ramos, Role of B5-type sites in Ru catalysts used for the NH3 decomposition reaction, Topics in catalysis 52 (2009) 758-764.

[34] Han, T., L. Wei, S. Xie, Y. Liu, H. Dai, and J. Deng, Catalyst design for ammonia decomposition: an overview, Industrial Chemistry & Materials (2025).

[35] Yan, W., B. Liang, G. Bi, H. Zhuo, W. Wang, H. Duan, G. Xu, F. Wang, Y. Su, T. Zhang, X. Yang, and Y. Huang, Interfacial Regulation of Ru-Based Catalysts for the Enhanced Activity of Ammonia Decomposition, ACS Sustainable Chemistry & Engineering 12 (2024) 15024-15032.

[36] Maccarrone, D., C. Italiano, G. Giorgianni, G. Centi, S. Perathoner, A. Vita, and S. Abate, A Comprehensive Review on Hydrogen Production via Catalytic Ammonia Decomposition, (2025).

[37] Richard, S., A. Ramirez Santos, P. Olivier, and F. Gallucci, Techno-economic analysis of ammonia cracking for large scale power generation, International Journal of Hydrogen Energy 71 (2024) 571-587.

[38] Devkota, S., J.-Y. Cha, B.-J. Shin, J.-H. Mun, H.C. Yoon, S.A. Mazari, and J.-H. Moon, Techno-economic and environmental assessment of hydrogen production through ammonia decomposition, Applied Energy 358 (2024) 122605.

[39] Ogawa, T., M. Yoshida, and K. Ishihara, Techno-economic analysis on recent heterogeneous catalysts for ammonia synthesis, (2022).

[40] Lu, Z., B. Jiang, Z. Chen, J. Shi, D. Jing, Y. Lu, and M. Liu, Advancements in thermocatalytic ammonia decomposition for hydrogen production, The Innovation Energy 1 (2024) 100056-100051-100056-100015.

[41] Chu, P.-C., S.-Y. Kang, M.-L. Yu, Y.-P. Liu, Y.-H. Chen, Y.-C. Hsu, H. Lee, C.-Y. Chiang, H.-Y. Chang, W.-H. Hung, and W.-C. Lin, Ammonia decomposition and hydrogen production via novel FeCoNiCuMnO high-entropy ceramic catalysts, npj Clean Water 8 (2025) 92.

[42] Li, Y., K. Wang, Z. Wang, X. Wang, X. Chu, R. Zhang, S. Song, H. Zhang, and X. Wang, Ultra-Fast Synthesis of Composite Oxide-Supported Transition Metal Alloy as an Advanced Catalyst for Ammonia Decomposition, Advanced Energy Materials 15 (2025) 2405296.

[43] Yu, X., F. Yin, G. Li, J. Zhang, and B. Chen, Preparation of nickel aluminate supported Ni nanocatalyst and its catalytic activity for ammonia decomposition to produce hydrogen, International Journal of Hydrogen Energy 104 (2025) 184-192.

[44] Xu, G., C. Cai, and T. Wang, Toward Sabatier Optimal for Ammonia Synthesis with Paramagnetic Phase of Ferromagnetic Transition Metal Catalysts, Journal of the American Chemical Society 144 (2022) 23089-23095.

[45] Xu, G., L. Sun, and T. Wang, Demagnetizing Ferromagnetic Catalysts to the Sabatier Optimal of Haber–Bosch Process, JACS Au 4 (2024) 1405-1412.

[46] Saidi, W.A., W. Shadid, and G. Veser, Optimization of High-Entropy Alloy Catalyst for Ammonia Decomposition and Ammonia Synthesis, The Journal of Physical Chemistry Letters 12 (2021) 5185-5192.

[47] Ohtsuka, Y., C. Xu, D. Kong, and N. Tsubouchi, Decomposition of ammonia with iron and calcium catalysts supported on coal chars, Fuel 83 (2004) 685-692.

[48] Lu, B., L. Li, M. Ren, Y. Liu, Y. Zhang, X. Xu, X. Wang, and H. Qiu, Ammonia decomposition over iron-based catalyst: Exploring the hidden active phase, Applied Catalysis B: Environmental 314 (2022) 121475.
[49] Pelka, R., I. Moszyńska, and W. Arabczyk, Catalytic ammonia decomposition over Fe/Fe4N, Catalysis Letters 128 (2009) 72-76.
[50] Purcel, M., S. Berendts, L. Bonati, S. Perego, A. Müller, M. Lerch, M. Parrinello, and M. Muhler, Iron Nitride Formation and Decomposition during Ammonia Decomposition over a Wustite-Based Bulk Iron Catalyst, ACS Catalysis 14 (2024) 13947-13957.
[51] Chen, S., J. Jelic, D. Rein, S. Najafishirtari, F.-P. Schmidt, F. Girgsdies, L. Kang, A. Wandzilak, A. Rabe, D.E. Doronkin, J. Wang, K. Friedel Ortega, S. DeBeer, J.-D. Grunwaldt, R. Schlögl, T. Lunkenbein, F. Studt, and M. Behrens, Highly loaded bimetallic iron-cobalt catalysts for hydrogen release from ammonia, Nature Communications 15 (2024) 871.
[52] Perego, S., M. Purcel, Y. Baum, S. Chen, A.S. Müller, M. Parrinello, M. Behrens, M. Muhler, and L. Bonati, No Time for Nitrides: How Cobalt Alloying Promotes Iron Catalysts for Ammonia Decomposition, ACS Catalysis 15 (2025) 16690-16702.
[53] Varadwaj, P.R., H.M. Marques, and I. Grabowski, Ammonia Synthesis over Transition Metal Catalysts: Reaction Mechanisms, Rate-Determining Steps, and Challenges, International Journal of Molecular Sciences 26 (2025) 4670.
[54] Gao, Y., E. Hu, Y. Yi, G. Yin, and Z. Huang, Plasma-assisted low temperature ammonia decomposition on 3d transition metal (Fe, Co and Ni) doped CeO2 catalysts: Synergetic effect of morphology and co-doping, Fuel Processing Technology 244 (2023) 107695.
[55] He, H., C. Chen, C. Bian, J. Ren, J. Liu, and W. Huang, Enhanced ammonia decomposition by tuning the support properties of Ni/GdxCe1-xO2-δ at 600° C, Molecules 28 (2023) 2750.
[56] Weissenberger, T., R. Zapf, H. Pennemann, and G. Kolb, Catalyst coatings for ammonia decomposition in microchannels at high temperature and elevated pressure for use in decentralized and mobile hydrogen generation, Catalysts 14 (2024) 104.
[57] Wang, L., L. Wang, X. Meng, and F.-S. Xiao, New Strategies for the Preparation of Sinter-Resistant Metal-Nanoparticle-Based Catalysts, Advanced Materials 31 (2019) 1901905.
[58] Hu, X., B. Guan, J. Chen, Z. Zhuang, C. Zheng, J. Zhou, T. Su, C. Zhu, S. Zhao, J. Guo, H. Dang, Y. Zhang, Y. Yuan, C. Yi, C. Xu, B. Xu, W. Zeng, Y. He, Z. Wei, and Z. Huang, Research status and advances of catalysts for hydrogen production from ammonia decomposition: Refined regulation methods, Fuel 381 (2025) 133134.
[59] Medford, A., A. Vojvodic, J. Hummelshøj, J. Voss, F. Abild-Pedersen, F. Studt, T. Bligaard, A. Nilsson, and J. Nørskov, ChemInform Abstract: From the Sabatier Principle to a Predictive Theory of Transition-Metal Heterogeneous Catalysis, Journal of Catalysis 328 (2015).
[60] Kang, B., Z. Chang, R. Zhang, Z. Shen, K. Wang, X. Guo, H. Wu, D. Li, D. Liu, Y. Wei, J. Jia, and Z.-j. Wang, Synergistic catalysis of CoN sites and Co nanoparticles for efficient COx-free hydrogen production from ammonia decomposition, Fuel 396 (2025) 135311.
[61] Dong, X., S. Zhu, and H. Li, Recent research progress of catalysts for thermocatalytic ammonia decomposition, International Journal of Hydrogen Energy 143 (2025) 286-306.
[62] Ji, H., X. Tang, L. Fu, J. Li, Z. Zheng, C. Ding, Y. Zhang, and C. Huang, Study on the Catalytic Effect of Nano Copper Oxide with Different Particle Sizes on the Thermal Decomposition of Ammonium Perchlorate, Catalysts 15 (2025) 882.

[63] Wu, M., F. Dong, Y. Yang, X. Cui, X. Liu, Y. Zhu, D. Li, S. Omanovic, S. Sun, and G. Zhang, Emerging Atomically Precise Metal Nanoclusters and Ultrasmall Nanoparticles for Efficient Electrochemical Energy Catalysis: Synthesis Strategies and Surface/Interface Engineering, Electrochemical Energy Reviews 7 (2024) 10.

[64] Liu, H., R. Zhang, S. Liu, and G. Liu, CeO2/Ni Inverse Catalyst as a Highly Active and Stable Ru-free Catalyst for Ammonia Decomposition, ACS Catalysis 14 (2024) 9927-9939.

[65] Li, X.-C., T.-T. Huang, Y. Hu, X. Li, Y.-F. Liu, H. Dong, C.-J. Jia, G.-S. Li, and Y.-W. Zhang, Enhancing metal-support interactions in CeAlOx/Co inverse catalyst for significantly boosting ammonia decomposition reaction, Applied Catalysis B: Environment and Energy 366 (2025) 125020.

[66] Ahn, S.-Y., W.-J. Jang, J.-O. Shim, B.-H. Jeon, and H.-S. Roh, CeO2-based oxygen storage capacity materials in environmental and energy catalysis for carbon neutrality: extended application and key catalytic properties, Catalysis Reviews 66 (2024) 1316-1399.

[67] Li, T., J. Zuo, Z. Zhao, W. Li, K. Zhang, Q. Wang, H. Du, H. Liu, E. Aili, and Y. Ye, Hydrogen production by ammonia decomposition: A strategy to enhance the activity and stability of metal catalysts, International Journal of Hydrogen Energy 97 (2025) 1153-1167.

[68] Purcel, M., A.S. Müller, P. Diehl, K. Kappis, A. Trunschke, and M. Muhler, Long-Term Stability of Ammonia Decomposition over Nickel-Based Catalysts, Energy Technology 13 (2025) 2400678.